Rotating Rayleigh-Bénard convection in cylindrical cells with aspect ratios one and two

Overkamp, J.V.

Award date:
2010

Rotating Rayleigh-Bénard convection in cylindrical cells with aspect ratios one and two

Jim Overkamp

July 2010
R-1770-A

Rotating Rayleigh-Bénard convection in cylindrical cells with aspect ratios one and two

Jim Overkamp

Applied Physics

Eindhoven University of Technology

July 2010

Supervisors
Prof. Dr. H.J.H. Clercx
Ir. R.J.A.M. Stevens

Graduation committee
Prof. Dr. H.J.H. Clercx
Dr. Ir. C.C.M. Rindt
Prof. Dr. F. Toschi
Dr. Ir. B.J.H. van de Wiel
Ir. R.J.A.M. Stevens

Abstract

Turbulent thermal convection occurs in numerous situations, for example in the Earth's atmosphere, in the Earth's liquid outer core and in turbo machinery. These systems can be represented by the rotating Rayleigh-Bénard problem, which is investigated experimentally with a newly designed cylindrical convection cell. The aspect ratio Γ of the cylindrical volume is defined as the ratio of its diameter and its height. Of interest in this study are the enhancement of heat transport between the upper and lower boundary due to rotation and the presence of a large-scale circulation in the contained fluid.

For this purpose, a new experimental setup is constructed, with an inner diameter of 250 mm and two different sidewall heights, resulting in aspect ratios Γ=1 and Γ=2. The lower boundary is a copper plate heated electrically, while the upper boundary is a copper plate cooled with water. Heat loss at the sidewalls is minimized with active and passive isolation. The profile of the large-scale circulation is measured using 16 or 24 temperature sensors in the sidewall and the heat transported is measured from the input power of the lower plate. The experiments with both aspect ratios are performed with water at a fixed Prandtl number of 4.38, at three different Rayleigh numbers of $2.99 \cdot 10^8$, $5.88 \cdot 10^8$ and $1.16 \cdot 10^9$.

Non-rotating measurements of heat transport for Γ=1 agree very well with measurements found in literature. The heat transport in Γ=2 is 6% lower, which is attributed to the more elliptical shape of the large-scale circulation. Heat transport is increased with up to 15% by rotation for Γ=1, which agrees with literature data in terms of position and magnitude, and up to 20% for Γ=2. The onset of rotational enhancement of heat transport is located at $Ro \approx 2$ for Γ=1, but at $Ro \approx 7$ for Γ=2. This is likely caused by the weaker large-scale circulation being more easy to overcome by Ekman pumping in the Γ=2 case, shifting the transition to higher Rossby numbers for higher aspect ratios.
The single-roll large-scale circulation is dominant in both aspect ratios at none to weak rotation. The disappearance of this mode coincides with the onset of rotational enhancement of heat transport, with the transition being sharper in Γ=2 than in Γ=1.

Overall, rotational heat transport enhancement showed expected behaviour for Γ=1, but revealed a so far undocumented aspect ratio dependence as supported by the Γ=2 measurements.

Contents

Chapter 1: Introduction 1

Chapter 2: Theory 5
2.1 Rayleigh-Bénard convection 5
2.1.1 Governing equations 6
2.1.2 Large-scale circulation 8
2.1.3 Boundary layers 9
2.2 Rotating Rayleigh-Bénard convection 10
2.2.1 Ekman layers 11
2.2.2 Ekman pumping 12

Chapter 3: Experimental setup 15
3.1 Convection cell 15
3.2 Rotating Table Facility 18
3.3 Measurement arrangement 20
3.3.1 Control parameters 20
3.3.2 Measurements 21
3.4 Data processing 22
3.4.1 Heat transport 22
3.4.2 Large-scale circulation 25
3.5 Measurement plan 25

Chapter 4: Results 29
4.1 Heat transport 29
4.1.1 Static experiments 29
4.1.2 Rotating experiments 30
4.2 Large-scale circulation 33
4.2.1 LSC intensity 33
4.2.2 LSC orientation preference 36

Chapter 5: Conclusion 39
5.1 Acknowledgements 40

References 41

Appendix A: Measurement data 43
A.1 Static experiments 43
A.2 Rotating experiments 44

Appendix B: Photos 47
B.1 Construction 47
B.2 Measurements on the Rotating Table Facility 48

Chapter 1: Introduction

Turbulent thermal convection is a key component in several flow configurations in nature and technology, yet the scientific knowledge of it is rather limited. This graduation project reports on an experimental study on a small part of the problem, namely heat transfer enhancement in rotating Rayleigh-Bénard convection.

Thermal convection occurs for example in the Earth's atmosphere. In the tropics, the light of the Sun heats the Earth's surface, causing the air above it to rise. At higher altitudes, this causes convective clouds [1]. Another geophysical example is deep ocean convection, where currents and atmospheric forcing collaborate to weaken stratification and allow surface water to sink to great depths [2]. These convection cells play a role in the thermohaline circulation, the large circulation current in the oceans which has a significant effect on the Earth's climate.
On even larger scales, thermal convection is present in the outer core of the Earth and other planets [3][4]. The flow in that region is thought to consist of irregularly distributed columnar vortices, but direct observations are absent. Combined with the conductive properties of the fluid, the flow in the outer core is responsible for the Earth's magnetic field [5].
Thermal convection also appears in advanced technology concerning heat transport. For example, the blades found in turbo machinery warm up considerably, and need to be cooled to ensure proper operation. Since the blades are rotating at high speed, heat transport differs from the regular non-rotating case [6]. Chemical vapour deposition (CVD) chambers, used for growing thin films on substrates, operate at increasing pressure and gas flow rates, which brings the system closer to flow patterns dominated by turbulent thermal convection [7]. The turbulent regime is often avoided because of the sense of uncontrollability, but it can increase the heat transport and mixing uniformity, thereby increasing the productivity of the reactor.

To investigate the thermal convection systems mentioned, a model is required which eliminates most of the complex and unknown factors, while still maintaining the essence of the problem. A minimal requirement is obviously the presence of a fluid. In all geophysical and astrophysical systems mentioned earlier, the fluid is exposed to a temperature gradient, so a hot and a cold boundary must be present. More specifically, the cold boundary must be the upper boundary of the fluid and the hot one the lower, resulting in a temperature gradient parallel to gravitation in the system. The temperature difference is expressed with the Rayleigh number. The fluid should

respond to the temperature difference, so its density needs to be a function of temperature.
The resulting flow model is based on a viscous fluid with temperature-dependent density between an upper, cold boundary and a lower, hot boundary in a gravitational system. In the simplest models no lateral confinement is present, so the upper and lower boundaries stretch out into infinity, or form a closed surface around the centre of gravitation like the mantle of the Earth. Of interest in this problem is the fluid motion between the plates, and the heat transported between the hot and the cold boundary as a result of that motion. The amount of heat transported is expressed with the Nusselt number. This model is called the Rayleigh-Bénard system.

If the temperature of the hot boundary is equal to that of the cold boundary, the whole system will be in static equilibrium. Slightly increasing the temperature difference between the boundaries will result in a heat flux from the hot boundary to the cold one. The fluid between the boundaries is still at rest, so the heat transport is solely due to the ability of the fluid to conduct heat.
Starting at a certain critical Rayleigh number, thus at a certain temperature difference, the temperature-dependent density of the fluid will come into play. The lower, warmer fluid near the hot boundary will have a lower density than the rest of the fluid, resulting in a localized upward flow. Similarly, near the top boundary cold fluid will start to fall and create a downward flow. The position at which these upward and downward flows occur is random, at least initially. Once the upward, warm flow reaches the upper, cold boundary, there is little probability of the fluid being cold enough to directly fall down again. Since the same reasoning applies on cold fluid near the hot boundary, the flow will show a general pattern: warm upward flow on one side and cold downward flow on the opposite side, forming a circulation. Since the fluid is now in motion, it no longer has to rely on just heat conduction to transport heat between the boundaries. The heat can be transferred by hot and cold fluid traveling to the opposite boundary, called convection. This convection, which is driven by the temperature difference of the boundaries, enables the system to transport far more heat between the boundaries than with just conduction.
A second transition occurs when adding rotating to this system, with the rotation vector anti parallel to the gravitational force. The inverse of the rotation rate is expressed as the Rossby number. Very slow rotation hardly has any impact on the flow; the circulation persists. Decreasing the Rossby number to below a critical value, so rotating faster than a critical rotation rate, will induce a transition in the flow: the circulation is suppressed and tubes of swirling fluid start to shoot away from the boundaries. These vortical tubes can, in a certain range of parameters, increase the heat transport with some 10 to 20% over the non-rotating case. However, beyond a certain rotation rate, velocity fluctuations become strongly damped due to the Taylor-Proudman effect, so convective heat transport will start to drop far down again.

The two transitions described above, one for a critical Rayleigh number and one for a critical Rossby number, are of great interest when trying to understand the Rayleigh-Bénard system. One of the methods to investigate these transitions is building an experimental reproduction of the Rayleigh-Bénard model and performing measurements with it.
A typical Rayleigh-Bénard setup consists of two circular plates, which serve as top and bottom boundaries for the fluid. Their diameter can reach from several centimeters to several meters. The plates are usually chosen to be made of copper or

other metals, since their ability to transport heat should be very high. The boundaries are temperature-controlled, and the power required to keep them at the same temperature represents the exact amount of heat the fluid is transporting between the plates. For the fluid, often water or air is used because of their ease of use. Because it is experimentally impossible to create infinitely extended top and bottom boundaries, a lateral confinement is required. As the fluid should transport heat only between the two plates, the sidewall should be made of a well-isolating material, like Perspex or another type of plastic. The ratio of the height of the sidewall and the diameter of the top and bottom plates can be crucial, since it determines how many circulations will be present in the fluid. A common choice is a height equal to the diameter of the plates, which results in an aspect ratio of 1. Using a smaller height of the sidewall gives a more circulation rolls side-by-side and increases the aspect ratio, while higher sidewalls give lower aspect ratios. The axis of rotation coincides with the axis of the cylinder.

The Rayleigh-Bénard problem has been a topic of intense research, especially with the increasing ability to perform numerical simulations on it. Experimental research started in 1900 with the first observations of convection cells by Bénard [8], followed by a theoretical analysis or the Rayleigh-Bénard problem with infinitely wide boundaries by Lord Rayleigh [9]. Half a century later, in the 1960s, Chandrasekhar improved this analysis by using perturbation theory and determined the critical Rayleigh number [10], while Rossby experimentally added background rotation to the problem [11]. It was Rossby who first observed the remarkable heat transfer enhancement due to background rotation.
Static experiments are used to investigate the transition from conduction to convection and the properties of the convective circulation. For example, in 1996, Chavanne et al. [12] published results from their onset of convection in helium at 4 K. The cell used in this case had a diameter of 10 cm and a height of 20 cm, and was immersed in liquid helium. Their aspect ratio was 0.5 rather than infinity, so the onset occurred at a different position than calculated by Chandrasekhar. Recently, Sun et al. [13] reported on experiments with water in a cell with a diameter of 1 meter, with aspect ratios ranging from 2/3 to 20, and Funfschilling et al. [14] published results on measurements in aspect ratio 1 at different sizes. Those experiments were performed to test the model which Grossmann and Lohse [15] developed to describe the relationship between temperature difference and heat transport. In particular, they theoretically derived scaling relations for the heat transport and the intensity of the circulation as a function of fluid properties and forcing parameters. More recently, Ebert et al. [16] investigated the temperature near the boundaries in a rectangular Rayleigh-Bénard system filled with air. The structure of the temperature profile proved to have three distinct, different regions. Xi et al. [17] performed measurements on the time-dependent behaviour of the convective circulation, which wanders around its mean position and appears to reverse at irregular intervals. In addition, the effects of using copper plates instead of perfectly conducting boundaries are explored numerically by Verzicco [18], and a correction method has been formulated. Brown et al. [19] verified and improved this method experimentally, using different sets of plates.
Rotating Rayleigh-Bénard experiments then try to gain understanding of the heat transfer enhancement by rotation, and attempt to seek the optimal conditions for it. To date, only few experiments have been performed on this transition, for example by Zhong et al. [20] and Kunnen [21]. Both report on an increase in heat transport at modest rotation in systems with aspect ratio 1. In addition, Kunnen et al. [22][23] were able to

investigate the circulation in the system and the turbulence statistics with Stereo Particle Image Velocimetry (SPIV), showing the lagging of the circulation at low rotation rates.
Simulations of rotating Rayleigh-Bénard convection have been performed as well. Since the flow is driven by turbulence, Direct Numerical Simulations (DNS) are required to capture all relevant aspects, making the simulations rather costly in terms of computer power. Stevens et al. [24] investigated the transition to heat transport enhancement and the disappearance of the circulation under rotation. Kunnen et al. [25] reported that under modest rotation, there is a velocity normal to the top and bottom boundaries. Though the enhancing effect of rotation is known, Zhong et al. [20] showed that the presence of it depends on fluid properties, in particular on the Prandtl number, the balance between viscosity and thermal diffusivity, of the fluid used.

Summarizing, there is knowledge about the two states of the non-rotating system and the transition between them, and about the existence of heat transfer enhancement by rotation. This enhancement and the coinciding disappearance of the circulation as hypothesized to be the result of Ekman pumping, but much further research is required to provide a solid understanding of this transition. Reverting to the astrophysical and geophysical occurrences of the Rayleigh-Bénard problem, it remains unclear what aspect ratio is required to sufficiently approach the infinitely wide system. It is difficult to create very large experimental systems, especially if they are to be tested on rotational effects. Another point of interest is the temperature difference in astrophysical systems; so far, experimental and numerical research have not been able to reach the same Rayleigh number, and an additional transition in the boundary layers is believed to currently separate these two cases [26].
Of all these remaining questions, this report will investigate the first one. An experimental Rayleigh-Bénard system is placed in a rotating frame of reference, and the heat transfer enhancement and the presence of the circulation will be measured. Even more, the experiments will be performed for two systems with different aspect ratios, allowing the effects of system geometry on heat transport and Ekman pumping to be made visible. As said, rotating Rayleigh-Bénard experiments have not been done often for aspect ratio one, but the experiments for aspect ratio two in this report will be the first in this field of research.

This report will first present some theory on the equations of motion in regular Rayleigh-Bénard convection. Next, the effects of background rotation are incorporated in the equations. Background rotation implicates the formation of Ekman layers near the top and bottom plates. The third chapter will introduce the new-built setup with which the Rayleigh-Bénard problem will be investigated under static and rotating conditions. In addition, the sensor configuration and data processing will be explained, and a plan for the measurement to be performed is introduced. Chapter four will discuss heat transport in the non-rotating case, and heat transport enhancement in the rotating case, for aspect ratios 1 and 2. After that, the intensity of the large-scale circulation and its orientation are presented. The final chapter will review and conclude the results. The appendices contain relevant measurement data and a selection of the photos made during this research.

Chapter 2: Theory

The Rayleigh-Bénard problem will be described first, complete with the governing equations, followed by an explanation of the different effects and boundary layers occurring in the rotating Rayleigh-Bénard system.

2.1 Rayleigh-Bénard convection

The Rayleigh-Bénard problem consists of two parallel boundaries at different temperatures enclosing a fluid layer. In the original experiments, performed by Henri Bénard in 1900, a fluid film on a metal heated plate was used, with the air above it being the upper boundary (see Figure 2-1) [8]. Bénard was interested in the effects of viscosity on this case, so he performed these experiments with a variety of fluids.

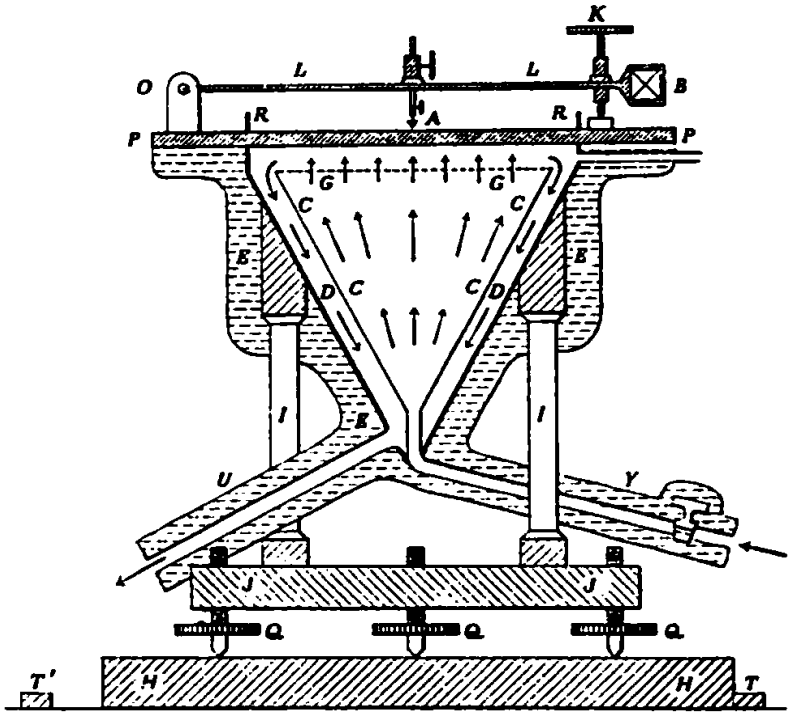

Figure 2-1: Schematics of the experimental setup Bénard used to investigate fluid films on a heated plate [10]. The fluid is between ridges R on levelled plate P.

If the temperature gradient between the two boundaries is only minor, the fluid will be unstably stratified, but buoyancy is not able to overcome viscous forces yet. Once the temperature gradient exceeds a certain critical value, buoyancy is able to overcome

them, resulting in convection cells, as illustrated in Figure 2-2. Bénard observed a pattern of hexagonal cells, with rising fluid at the center and descending fluid at the cell boundaries (see Figure 2-3), but other shapes, such as rolls and rectangles, are possible as well [10].

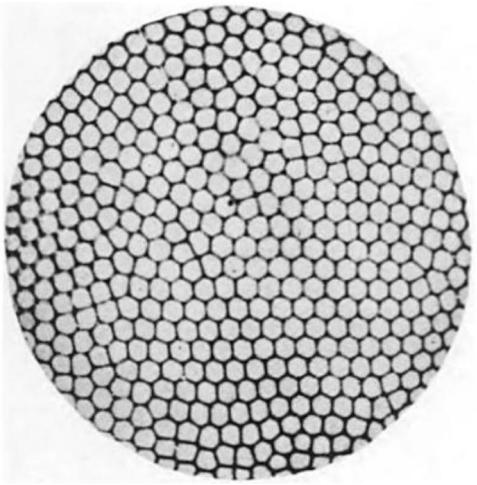

Figure 2-2: Reproduction of Bénards photograph of a convection cell pattern in a fluid layer [10].

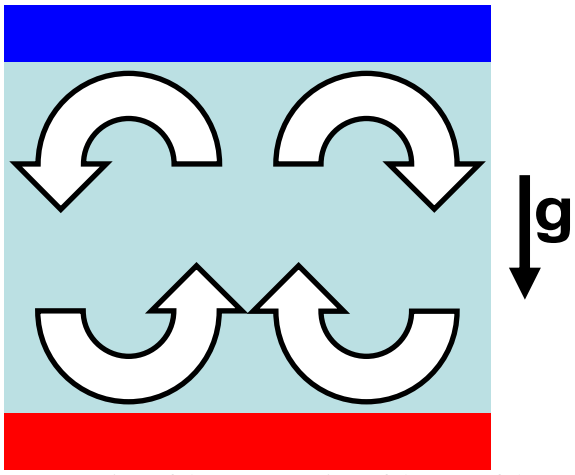

Figure 2-3: Schematic representation of the cross-section of the one of the cells observed by Bénard.

2.1.1 Governing equations

Some years later, Lord Rayleigh theoretically analyzed this convective instability [9]. The incompressible flow of the Newtonian fluid between the boundaries is governed by the incompressible Navier-Stokes equations,

$$\nabla \cdot \vec{u} = 0\,, \tag{2.1}$$

$$\frac{\partial \vec{u}}{\partial t} + (\vec{u} \cdot \nabla)\vec{u} = -\frac{1}{\rho}\nabla p + \vec{g} + \nu \nabla^2 \vec{u}\,. \tag{2.2}$$

Combined with the energy equation and the Boussinesq approximation (buoyancy is negligible, except in the gravitational term), this produces

$$\nabla \cdot \vec{u} = 0\,, \tag{2.3}$$

$$\frac{\partial \vec{u}}{\partial t} + (\vec{u} \cdot \nabla)\vec{u} = -\beta T\vec{g} - \frac{1}{\rho_0}\nabla p + \nu \nabla^2 \vec{u}\,, \tag{2.4}$$

$$\frac{\partial T}{\partial t} + (\vec{u} \cdot \nabla) T = \kappa \nabla^2 T \,. \tag{2.5}$$

In these equations, $\vec{u}$ is the velocity field, β the thermal expansion coefficient of the fluid, T the temperature, $\vec{g}$ the gravitational acceleration, ρ the fluid density, ρ_0 the mean fluid density, p the pressure, ν the kinematic fluid viscosity and κ the thermal diffusivity of the fluid. The flow can be characterized using dimensionless numbers,

$$Ra = \frac{\beta g \Delta L^3}{\kappa \nu}, \tag{2.6}$$

$$Pr = \frac{\nu}{\kappa}, \tag{2.7}$$

named the Rayleigh and Prandtl, respectively. In these definitions, Δ is the temperature difference between the two boundaries and L the distance between these boundaries. The Rayleigh number represents the ratio of the buoyancy forces and the thermal and momentum diffusivities, while the Prandtl number is the ratio of these thermal and momentum diffusivities. The Nusselt and Reynolds number are defined, respectively, as,

$$Nu = \frac{QL}{\lambda \Delta}, \tag{2.8}$$

$$Re = \frac{UL}{\nu}, \tag{2.9}$$

with λ the thermal conductivity coefficient of the fluid, Q the heat transported through the fluid and U the mean fluid velocity. The Nusselt number shows the ratio of the convective and the conductive heat transfer through a medium and the Reynolds number is the ratio of inertial forces and viscous forces. These numbers are a result of the setup and the chosen Rayleigh and Prandtl numbers.

In the experimental Rayleigh-Bénard problem, the fluid used can be chosen freely. The mean temperature of the fluid and the temperature difference between the boundaries are usually chosen to be adjustable, which stems from the temperature-controlling nature of experimental equipment. The mean temperature combined with the fluid choice determines the Prandtl number. The deviations from the mean temperature as a result of the temperature difference between the boundaries are sufficiently small to safely assume the Prandtl number remains constant in the complete Rayleigh-Bénard problem. The fluid choice, the temperature difference and the height of the setup then determine the Rayleigh number. The heat transport, expressed in the Nusselt number, is an unknown function of the Rayleigh and Prandtl number. If the fluid is stratified, the heat transport is purely conductive and the Nusselt number is equal to unity. Above a certain critical temperature difference, thus above a critical Rayleigh number, the fluids starts to move vertically, resulting in convective heat transport and increasing the Nusselt number above unity.

Using first-order perturbation theory and substitution of normal modes, Chandrasekhar was able to analyze the stability of the stratified system in the 1960s. The analytically derived critical value of 1707.8 for the Rayleigh number for the Rayleigh-Bénard problem with two infinitely wide, rigid boundaries coincides very well with experiments by Silveston on the onset of the convection cells, as shown in Figure 2-4 [10].

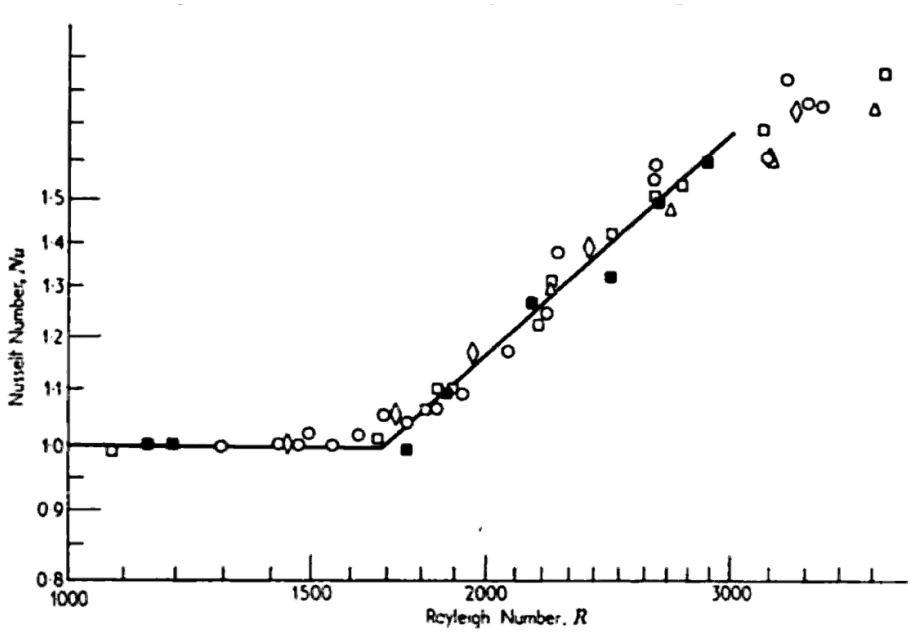

Figure 2-4: Experimental data by Silveston for the onset of convection in silicon oil (solid squares and open diamonds), ethylene glycol (open squares), heptane (open triangles) and water (open circles) [10].

2.1.2 Large-scale circulation

At Rayleigh numbers higher than the critical value, the fluid will start to move and transport heat. From small disturbances near the lower, hot boundary, plumes of warm fluid emerge. These plumes rise, because their density is lower than that of the colder fluid above them. When they impact on the top plate, they generate small disturbances on the upper, cold boundary, resulting in cold plumes travelling downward via the same mechanism. In both cases, the plumes try to heat the upper plate and cool the lower plate; the fluid is convectively transporting heat. Gradually, the plumes will group together, with warm plumes on one side of the cell and cold ones at the other. This creates a stable circulation pattern between the boundaries, named the large-scale circulation (LSC), as illustrated in Figure 2-5 [27].

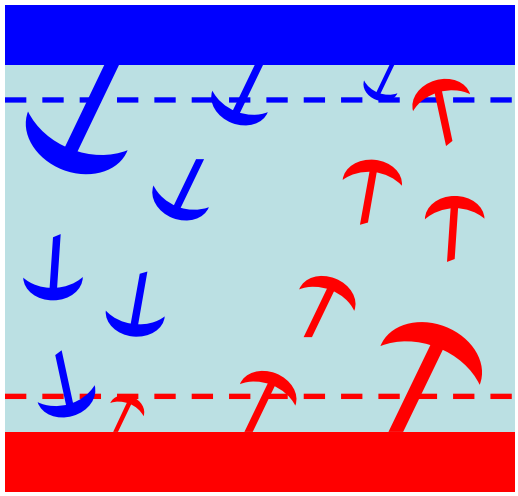

Figure 2-5: Schematic illustration of plumes detaching from the boundaries of a Rayleigh-Bénard cell to transport heat and create a large-scale circulation. The boundary layers are indicated with dashed lines [27].

With the appearance of an LSC, the temperature profile between the boundaries changes. Since the bulk fluid circulates, the temperature gradient will be concentrated mainly on the boundary layers, as shown in Figure 2-6.

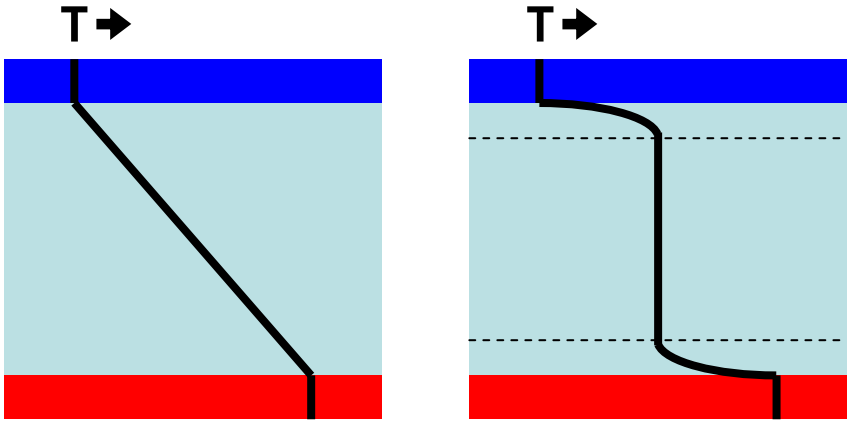

Figure 2-6: Schematic temperature profiles between the boundaries for the purely conducting case (left) and the largely convective case (right).

2.1.3 Boundary layers

In the presence of a flat boundary, the complete solution of (2.1)-(2.2) can be approximated by a separation into two regions: the inviscid interior and the friction-dominated boundary layer. The boundary layer method makes use of the notion that the velocity normal to the wall is much smaller than the velocity parallel to the wall, allowing the resulting boundary layer equations to be solved (semi-)analytically. For a two-dimensional case, the equations for a viscosity-dominated steady boundary layer are

$$\begin{aligned} &\frac{\partial u}{\partial x}+\frac{\partial v}{\partial y}=0 \\ &u\frac{\partial u}{\partial x}+v\frac{\partial u}{\partial y}=-\frac{1}{\rho}\frac{\partial p}{\partial x}+\nu\left(\frac{\partial^2 u}{\partial x^2}+\frac{\partial^2 u}{\partial y^2}\right). \\ &u\frac{\partial v}{\partial x}+v\frac{\partial v}{\partial y}=-\frac{1}{\rho}\frac{\partial p}{\partial y}+\nu\left(\frac{\partial^2 v}{\partial x^2}+\frac{\partial^2 v}{\partial y^2}\right) \end{aligned} \tag{2.10}$$

The velocity parallel to the wall, u, is much larger than the velocity normal to the wall, v. In addition, variations in velocity and pressure along the wall are much smaller than variations normal to the wall. Using this on (2.10) produces the following simplified set of equations

$$\begin{aligned} &\frac{\partial u}{\partial x}+\frac{\partial v}{\partial y}=0 \\ &u\frac{\partial u}{\partial x}+v\frac{\partial u}{\partial y}=-\frac{1}{\rho}\frac{\partial p}{\partial x}+\nu\frac{\partial^2 u}{\partial y^2}. \\ &0=-\frac{1}{\rho}\frac{\partial p}{\partial y} \end{aligned} \tag{2.11}$$

At a pressure which is constant normal to the wall, these equations reduce to

$$\begin{aligned} &\frac{\partial u}{\partial x}+\frac{\partial v}{\partial y}=0 \\ &u\frac{\partial u}{\partial x}+v\frac{\partial u}{\partial y}=\nu\frac{\partial^2 u}{\partial y^2} \end{aligned}. \tag{2.12}$$

The solution of these boundary layer equations can be matched smoothly with the solution for the inviscid interior, allowing the seemingly difficult problem to be solved with relative ease.

2.2 Rotating Rayleigh-Bénard convection

The rotating case of the Rayleigh-Bénard problem investigates a second transition in the system. The convections cells formed at sufficiently large Rayleigh numbers are meta-stable under static or slowly rotating conditions, but will be destroyed at a critical rotation rate. Once the convection cell is no longer the dominant structure, heat transport will predominantly occur through vortex tubes. At first, this moderately increases heat transport, but that effect disappears at higher rotation rates and the Nusselt number will drop considerably [11].

Adding rotation to the system induces fictitious forces, specifically the Coriolis force, turning (2.4) and (2.5) into

$$\frac{\partial \vec{u}}{\partial t}+(\vec{u}\cdot\nabla)\vec{u}+2\vec{\Omega}\times\vec{u}=-\beta T\vec{g}-\frac{1}{\rho}\nabla p+\nu\nabla^2\vec{u}\,, \tag{2.13}$$

$$\frac{\partial T}{\partial t}+(\vec{u}\cdot\nabla)T=\kappa\nabla^2 T\,, \tag{2.14}$$

with Ω the rotation rate in radians per second pointing in the positive z-direction and p the pressure, with absorbed centripetal force [28]. The rotation also adds another dimensionless number,

$$Ro=\frac{\sqrt{\beta g\Delta}}{\sqrt{L}\,2\Omega}. \tag{2.15}$$

This so-called Rossby number is the ratio of the inertial forces and the Coriolis force, and contains the free-fall velocity $U_{FF}=\sqrt{\beta g\Delta L}$. The inverse relation with the rotation rate means high rotation rates result in small Rossby numbers.

Another fictitious force induced by rotation is the centrifugal force. The dimensionless number representing the importance of the centrifugal force compared to buoyancy effects is the Froude number, defined as

$$Fr=\frac{\Omega^2 D}{2g}, \tag{2.16}$$

with D the horizontal dimension of the system. The equations (2.13) and (2.14) are only valid if the centrifugal forces are negligibly small, thus only when the Froude number is far smaller than unity.

The momentum equation (2.13) can be made dimensionless by defining $\vec{u}' = \vec{u}\frac{1}{U}$, $p' = p\frac{1}{\rho U^2}$, $\vec{g}' = \vec{g}\frac{L}{U^2}$, $\nabla' = \nabla L$, $T' = T\frac{1}{\Delta}$ and $\frac{\partial}{\partial t'} = \frac{L}{U}\frac{\partial}{\partial t}$, with U the characteristic velocity, which yields, directly dropping the primes for convenience of notation,

$$\frac{\partial \vec{u}}{\partial t} + (\vec{u}\cdot\nabla)\vec{u} + \frac{1}{Ro}\hat{z}\times\vec{u} = -\beta T\vec{g} - \nabla p + \frac{1}{Re}\nabla^2\vec{u}\,, \tag{2.17}$$

using the Rossby and Reynolds numbers defined earlier and with $\hat{z}$ the unit vector in z-direction. Under geostrophic conditions, the bulk flow is stationary and frictionless, resulting in a balance between the gravitational and Coriolis forces on one side and the pressure gradient on the other, so (2.17) turns into

$$\frac{1}{Ro}\hat{z}\times\vec{u} = -\beta T\vec{g} - \nabla p\,. \tag{2.18}$$

Note that the Rossby number is assumed to be considerably smaller than unity, allowing the advective term to be neglected. In the z-direction, (2.18) reads

$$\beta T g = \frac{\partial p}{\partial z}, \tag{2.19}$$

with $g = |\vec{g}|$, which is the hydrostatic balance in temperature formulation. Taking the derivative of (2.18) in the z-direction and substituting (2.19) yields

$$\frac{1}{Ro}\hat{k}\times\frac{\partial \vec{u}}{\partial z} = -\beta\vec{g}\frac{\partial T}{\partial z} - \beta g\nabla T\,. \tag{2.20}$$

With $\frac{\partial w}{\partial z} = 0$, a result of (2.18) combined with (2.1), this can be rewritten as the thermal wind balance,

$$\frac{1}{Ro}\frac{\partial \vec{u}}{\partial z} = \beta g\hat{z}\times\nabla T\,. \tag{2.21}$$

This balance states that horizontal temperature gradients cause vertical velocity gradients. If, however, the flow is barotropic, density is a function of only the pressure, so the temperature gradient points in the z-direction. The thermal wind balance then turns into

$$\frac{\partial \vec{u}}{\partial z} = 0\,. \tag{2.22}$$

This constraint is named the Taylor-Proudman theorem, and forbids vertical variations in the velocity field. One result of this theorem is the presence of so-called Taylor columns, which are phantom obstacles generated above or below actual obstacles. In addition, this theorem does not state the vertical velocity has to be zero, solely that it has to be constant along the vertical direction.

2.2.1 Ekman layers

For rapidly rotating the systems, the boundary layers are dominated by the balance between the Coriolis force and friction. These layers were observed for the first time

on the Arctic, where icebergs propagated not in the direction of the predominant wind, but under an angle with it.
Consider a rapidly rotating system with a wall at $z=0$. For the inviscid bulk, (2.13) reduces to

$$2\vec{\Omega}\times\vec{u}_b = -\frac{1}{\rho}\nabla p_b\,, \tag{2.23}$$

with u_b the velocity in the bulk. In the boundary layer, the Rossby and Reynolds number are both very small, so (2.13) turns into

$$2\vec{\Omega}\times\vec{u}_E = -\frac{1}{\rho}\nabla p_E + \nu\frac{\partial^2\vec{u}_E}{\partial z^2}\,, \tag{2.24}$$

with u_E the velocity in the Ekman layer and under the assumption that horizontal variations in velocity are much smaller than the ones normal to the wall. The pressure in the boundary layer is identical to the pressure in the bulk, so

$$-\frac{1}{\rho}\nabla p_E = -\frac{1}{\rho}\nabla p_b\,. \tag{2.25}$$

Using (2.25) and (2.23) in (2.24) then yields

$$2\vec{\Omega}\times\vec{u}_E = 2\vec{\Omega}\times\vec{u}_b + \nu\frac{\partial^2\vec{u}_E}{\partial z^2}\,. \tag{2.26}$$

With the boundary conditions that u_E must be zero at the wall ($z=0$) and must match u_b far from the wall ($z\to\infty$), the solution to (2.18) is

$$\begin{aligned} u_E &= u_b - e^{-\zeta}\left[u_b\cos\zeta + v_b\sin\zeta\right] \\ v_E &= v_b + e^{-\zeta}\left[u_b\sin\zeta - v_b\cos\zeta\right] \end{aligned}, \tag{2.27}$$

where $\zeta = \frac{z}{D_E}$ is a coordinate change and D_E is a length scale defined as $D_E = \sqrt{\frac{\nu}{\Omega}}$.
The horizontal velocity in this boundary layer differs considerably from the flow in the bulk, both in magnitude and in direction [21].
The ratio of the momentum diffusivity and Coriolis forces is expressed as the dimensionless Ekman number,

$$Ek = \frac{\nu}{\Omega L^2}\,, \tag{2.28}$$

where large Ekman numbers indicate large Ekman layers. Note that the Ekman number is directly related to the boundary layer length scale found in (2.27), because $\frac{D_E}{L} = \sqrt{Ek}$.

2.2.2 Ekman pumping

The break-up of the LSC and the increase in heat transport in rotating Rayleigh-Bénard convection is hypothesized to be the result of Ekman pumping [25]. One of the peculiarities of Ekman layers is that, while they are thin compared to the bulk dimension, they are able to influence the flow in the bulk fluid through Ekman pumping.

The continuity equation (2.1) in the boundary layer is

$$\frac{\partial w_E}{\partial z} = -\left(\frac{\partial u_E}{\partial x} + \frac{\partial v_E}{dy} \right), \tag{2.29}$$

with u_E, v_E and w_E the velocity components. Since the expressions for the horizontal velocities are known, this produces

$$\frac{\partial w_E}{\partial z} = \left(\frac{\partial v_b}{\partial x} - \frac{\partial u_b}{\partial y} \right) e^{-\zeta} \sin \zeta \,. \tag{2.30}$$

The solution of this differential equation is

$$w_E = \frac{\sqrt{Ek}}{2} \left(\frac{\partial v_b}{\partial x} - \frac{\partial u_b}{\partial y} \right) \left[1 - e^{-\zeta} \left(\cos \zeta + \sin \zeta \right) \right]. \tag{2.31}$$

For this, conservation of mass (2.1) and the Taylor-Proudman theorem (2.22) applied on the bulk flow have been used. The boundary layer solution for the vertical velocity must still match the bulk vertical velocity, requiring

$$\lim_{\zeta \to \infty} w_E(\zeta) = \lim_{z \to 0} w(z) \,. \tag{2.32}$$

Applying (2.32) to (2.31) shows that

$$w(x, y, 0) = \frac{\sqrt{Ek}}{2} \left(\frac{\partial v_b}{\partial x} - \frac{\partial u_b}{\partial y} \right). \tag{2.33}$$

A horizontal bulk flow driven by a pressure gradient will induce a vertical velocity. Although there is an impenetrable wall at $z=0$, the boundary layer creates a non-zero vertical velocity as a boundary condition for the bulk flow, as shown in Figure 2-7. Combined with the Taylor-Proudman theorem (2.22), which forbids vertical variations in w in the bulk, this vertical velocity is able to penetrate the bulk fluid [29].

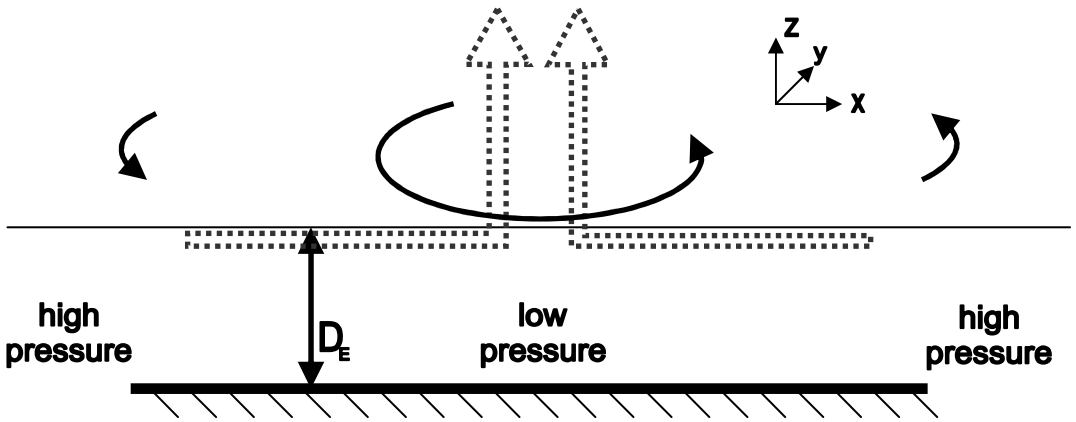

Figure 2-7: Schematic view of an Ekman layer 'pumping' fluid into the bulk.

The Ekman tubes are formed at the top of the kinetic boundary layer, as (2.31) shows. The amount of heat these tubes are able to transfer depends on the temperature of the fluid they transport, and on the heat diffusivity in the bulk. Very high Prandtl numbers indicate low heat diffusivity, so heat is flowing out of the tubes only slowly, but also a thermal boundary layer which is thinner than the kinetic boundary layer. This means that the fluid entering the tubes is hardly warmer than the bulk fluid. Very low Prandtl

numbers result in relatively hot fluid pumped upward, but this heat is quickly lost due to thermal diffusion. Both cases are illustrated in Figure 2-8.

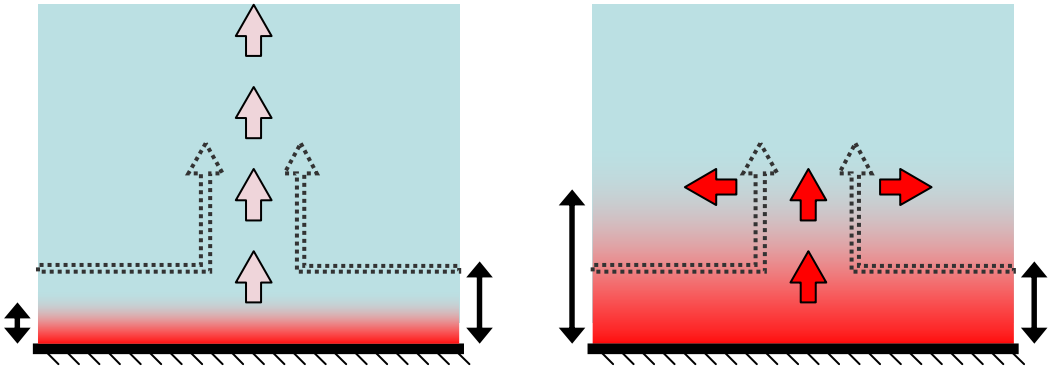

Figure 2-8: Schematic view of heat transport via Ekman pumping. Left is an illustration of the high-Prandtl case, with thin thermal boundary layers and low heat diffusion. Right is the low-Prandtl case, with thick thermal boundary layers and high heat diffusion.

A balance between these two effects, so pumping moderately warm fluid into the bulk with moderate heat diffusion, will provide optimal heat transport through Ekman pumping, illustrated in Figure 2-9.

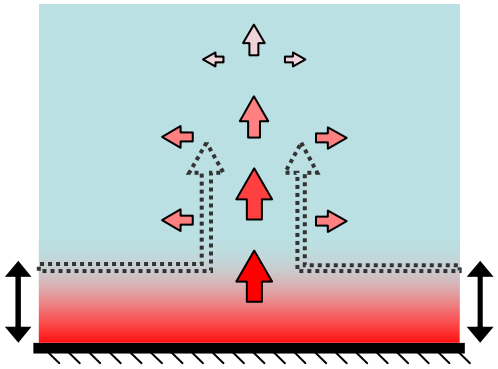

Figure 2-9: The intermediate-Prandtl case, for optimal heat transport through Ekman pumping.

Chapter 3: Experimental setup

The Rayleigh-Bénard problem posed in section 2.1 can be investigated experimentally using a precise setup. First, the convection cell design and construction will be described, followed by a brief description of the rotation facilities. Next, the setup of the sensors is discussed, and finally the data processing is explained.

3.1 Convection cell

The Rayleigh-Bénard problem consists of a fluid layer between two boundaries, of which the bottom boundary is at a higher temperature than the top one. In the experimental setup, water is enclosed between two round copper plates and a cylindrical Plexiglas sidewall, as shown in Figure 3-1. Copper, like other metals, has a high heat conduction coefficient, ensuring a temperature distribution along the plates that is close to uniform. In contrast, Plexiglas, a transparent thermoplastic, has a rather low heat conduction coefficient and will follow the temperature profile created by the flowing water while isolating it from external temperature gradients. The copper plates have ridges with rubber rings in them, which avoid any water or air leakage on the interface with the Plexiglas sidewall.

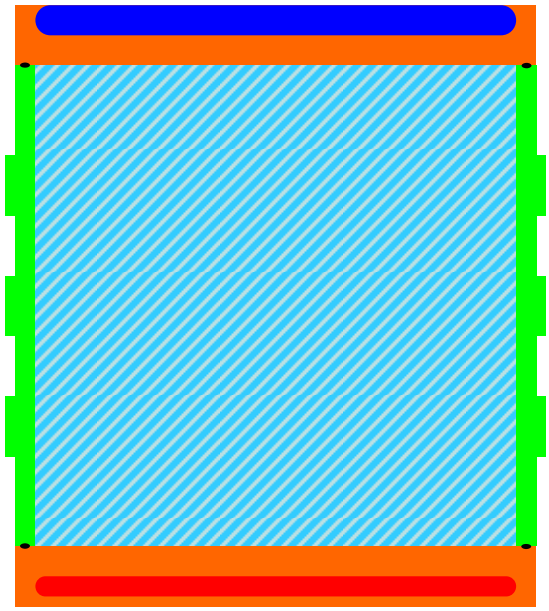

Figure 3-1: Schematic view of the convection cell. Water (light blue striped) is enclosed between two copper plates (orange) and and Plexiglas sidewall (green). The top plate is cooled using water (dark blue), the bottom plate is heated electrically (red).

The cylindrical volume enclosed by the plates and the sidewall has a diameter of 250 mm. The aspect ratio Γ (denoted as AR in graphs) is defined as the ratio of diameter D and the height L of the cell. To test the aspect ratio dependence of the Rayleigh-Bénard problem, sidewalls of two different heights are used, specifically L=250 mm (Γ=D/L=1) and L=125 mm (Γ=2). By extensively heating the water and removing all air bubbles, it is made sure that no air can affect the contact surface between the water and the plates.
The temperature gradient is created by heating the lower copper plate and cooling the top one, while keeping the mean of these temperatures at 40°C. The bottom plate is 30 mm thick 270 mm diameter pure copper and contains two 4 m long resistance wires (Inconel 600) in a spiralling pattern, as can be seen in Figure 3-2. Each wire has a resistance of 12.3 Ω and they are connected in parallel to a DC power supply, an Agilent 6675A, with a maximum rated power output of 2160 W. The temperature of the bottom plate can be controlled from room temperature up to 60 °C accurately. The top plate is 30 mm thick 270 mm diameter pure copper as well, but contains a single spiralling water channel of 26 mm deep and 8 mm wide, shown in Figure 3-2. The plate is connected to a Haake bath, a Thermo Fisher DC-50 heater and K41 refrigerator with a 15 litre reservoir, using two 9 mm diameter plastic tubes of approximately 3.90 m in length, with a water flow of about 12.5 litres per minute. The Haake bath is used refrigerate the water, so the top plate can be temperature controlled anywhere between 15 °C and 60 °C at heat fluxes exiting the top plate from 0 W to 1000 W. In both plates, the spiralling pattern ensures a high degree of uniformity in the surface temperature.

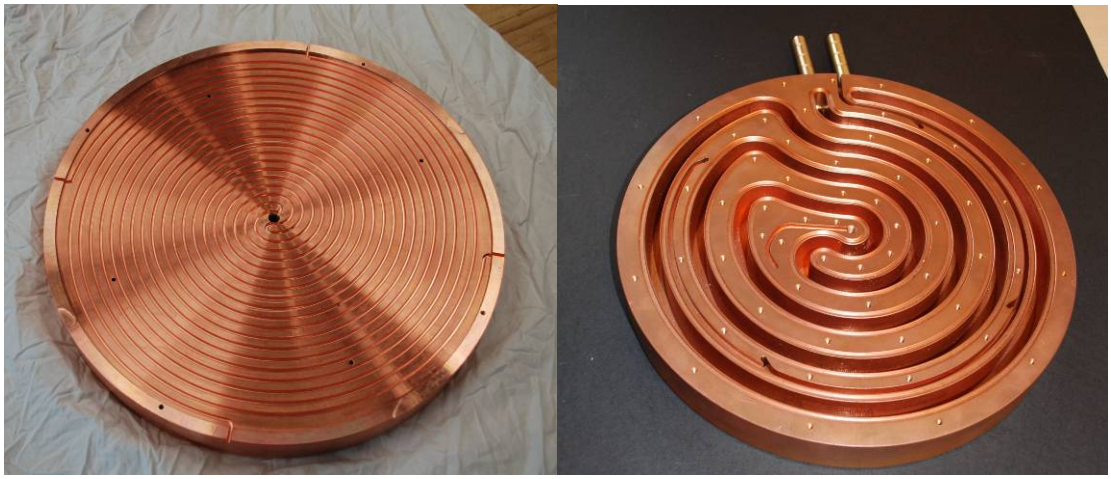

Figure 3-2: Photographs of the back of the bottom copper plate (left) and the top of the top copper plate (right). The bottom plate contains two resistance wires, the top plate a single water channel.

The quantity of interest in this experiment is the heat flux through the fluid. Measuring the heat flux in the fluid itself is not possible, so it has to be done at one of the plates. The cooling method of the top plate does not facilitate measurement of the absorbed power, but the bottom plate, with its electrical heating, allows for precise measurement of the dissipated power. The magnitude of the power is only equal to the heat flux through the fluid if all heat flows from the lower plate into the fluid to the top plate and no heat is lost at the sidewalls.
To achieve this condition, the system is actively isolated. The bottom plate is surrounded by three other, slightly larger buckets, as shown in Figure 3-3. A Eurotherm MINI8 controller combined with a solid-state relay, a 250 W heater and an RTD-based feedback loop is electronically keeping the middle bucket at the same

temperature as the copper bottom plate. Due to the absence of temperature gradients on the sides and bottom of the copper bottom plate, all heat flux will be passing through the fluid. The Plexiglas sidewall already has isolating properties, but is further isolated with three layers of plastic isolation and a 3 mm thick sheet of aluminium, also shown in Figure 3-3. Additionally, a number of 65 mm wide electronically heated ribbons are placed on the exterior of the aluminium sheet, keeping the entire sidewall isolation at approximately the mean temperature of the fluid thus reducing temperature gradients over the isolation. An RTD-based temperature sensor is placed on each ribbon, and every ribbon can be controlled separately up to a power of 75 W by the Eurotherm controller. This way, heat loss through the sidewall is minimized. The number of ribbons depends on the sidewall height, four were used for the Γ=1 experiment and two for the Γ=2 experiment. Despite the isolation efforts, 0.23 W of heat leakage is still present, which is determined from prescribing zero temperature difference between the copper plates and allowing the system to equilibrate for several days. This heat leakage is only a fraction of the total power dissipated in the experiments, and will be corrected for systematically.

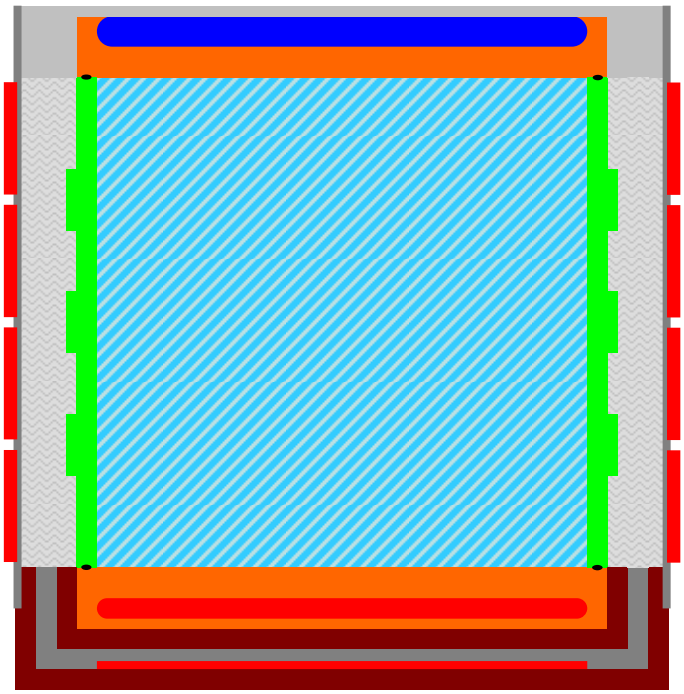

Figure 3-3: Schematic view of the convection cell with active and passive isolation (compare with Figure 3-1). The bottom plate is isolated with two layers of hard fiber (brown) and an actively heated aluminium bucket (dark grey). The sidewalls are isolated with plastic isolation (light grey), a 3 mm aluminium sheet (grey) and heating ribbons (red).

To increase the stiffness and rigidity of the setup, the whole system is placed on an aluminium plate and supported by an aluminium ring on stainless steel poles. The complete convection cell is shown in Figure 3-4.
Early tests showed that the remaining heat leakage of the setup depends heavily on the temperature in the laboratory. To reduce the impact of activity peaks in the air conditioning system and of the heat generated by the Haake bath, another layer of plastic isolation is wrapped around the setup and the whole setup is covered by a 63 x 68 x 61 cm³ wooden box, padded with 4 cm thick isolation on the inside. The maximum temperature drop, occurring at air conditioning activation on a regular

Monday morning, of 3 °C is decreased to 0.7 °C inside the wooden box, and is indiscernible in the isolation layer on the sidewall.

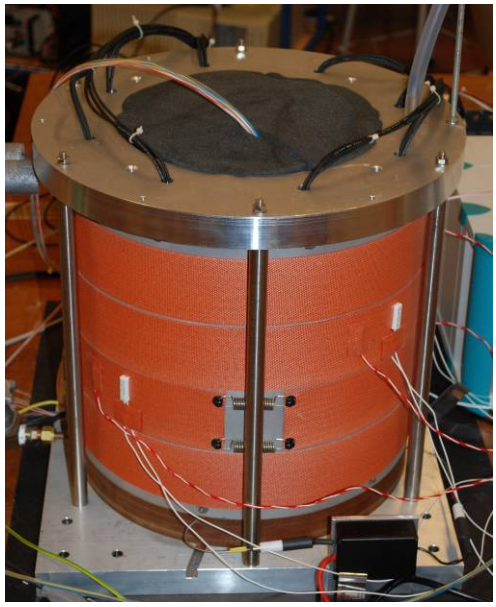

Figure 3-4: Photograph of the complete Γ=1 convection cell. Visible are the supporting poles, the heating ribbons (orange) and the aluminium sheets (grey, under the ribbons).

Additional images from the setup and its construction can be found in Appendix B.1.

3.2 Rotating Table Facility

In 2005, the Turbulence and Vortex dynamics group of the Eindhoven University of Technology started using a new Rotating Table Facility (RTF) [30], shown in Figure 3-5. Due to its size and the connections available on the rotating frame, the RTF is used for different kinds of experiments, including rotating Rayleigh-Bénard convection.

Figure 3-5: The Rotating Table Facility (RTF) at the Eindhoven University of Technology.

The static part of the table consists of a tripod foot, which is anchored to the ground. A single direct drive torque motor drives the rotation axis. A round aluminium table with a diameter of 1.75 m is mounted on top of the axis. To facilitate different constructions on the table, the table surface has a large number of regularly spaced M6 screw holes. Below the table are different racks to place electronic equipment. A rotating connection is available for coolant fluid, with separated in and out flow tubes. Using slip rings, three 3-wire serial connections are available for communication between the static and the rotating frame, as well as an optical 1 Gbps network interface. Power outlets are available on the rotating frame, with a total capacity of 6 kW.

The convection cell as described in section 3.1 is placed at the centre of the rotating table and fixed solidly. The setup is positioned mechanically, so the centre of the cylinder is off the rotating axis by no more than 0.1 mm. The power supply and the controller are placed on opposing sides on the rotating table, to keep the table loading close to symmetric. The Haake bath, used to cool the top plate in the experiment, is placed next to the table and connected using the coolant connection mentioned earlier. Due to its weight and the off-axis placement, the Haake bath cannot be placed in the rotating reference frame with the rest of the setup. The final setup is shown in Figure 3-6.

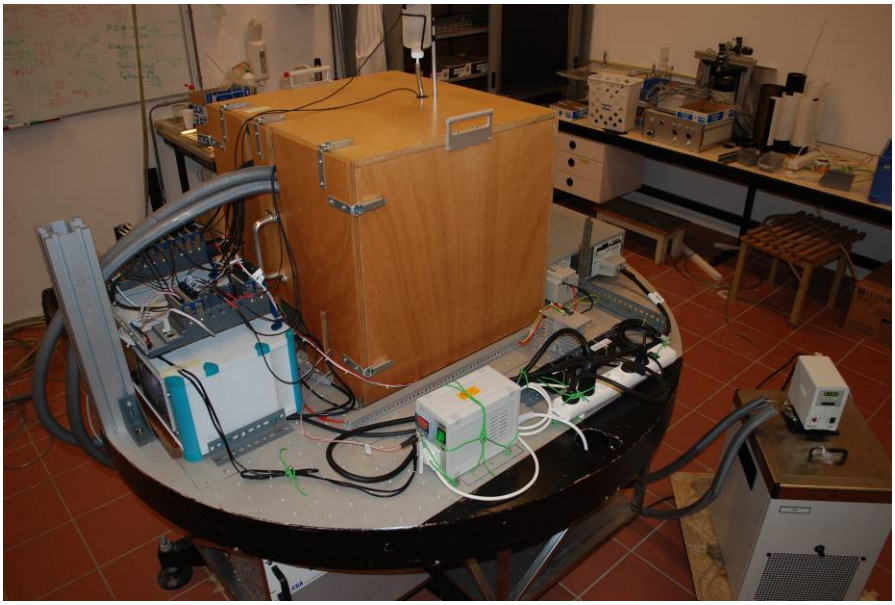

Figure 3-6: The Rayleigh-Bénard setup on the RTF. Visible are the Haake bath (bottom right, on the floor), the Eurotherm controller and CompactRIO system (left, described in section 3.3), the isolating wooden box (middle) and the Agilent power supply (behind the box).

The rotation rate of the RTF can be controlled from 0 to 10 radians per second with a resolution of 0.0001 radians per second and a relative accuracy of 0.5%. Both the RTF and the Rayleigh-Bénard setup are designed to operate properly without much user interaction, and both have software protections to cease operation in case of overheating or equipment malfunctioning.
Additional images from the setup on the RTF can be found in Appendix B.2.

3.3 Measurement arrangement

The entire setup is operated from a Windows XP PC running National Instruments LabView 8.6 connected to a National Instruments CompactRIO system and the Eurotherm control unit via 1 Gbps wired Ethernet. The PC can be remotely controlled via the Internet, facilitating tight measurement schedules. To perform accurate experiments with the Rayleigh-Bénard system, the temperature and temperature gradients at different locations are important, as well as several control parameters.

3.3.1 Control parameters

Foremost, the CompactRIO system controls the temperatures of the top and bottom plate. Both plates have a PT100-sensor at their centre, at 0.7 mm from the surface, connected to separate ADC channels on the CompactRIO system. The Haake bath, cooling the top plate, is controlled via an RS-232 interface, where the setpoint of the water temperature is automatically corrected for any heat loss along the water tubes, resulting in the desired temperature of the top plate. The Agilent power supply is controlled externally using a DAC on the CompactRIO system, ranging from 0 to -5 V in a double PID loop. The inner, faster loop regulates the dissipated power within a certain window; the outer, slower loop moves the centre of this window to account for slow changes. This way, the PID loop cannot overcompensate for turbulent effects in the flow, but is still able to respond to mean changes. Both controls succeed in regulating the temperature of the centre of the plates within 0.02 °C.
Additionally, the Eurotherm control unit regulates the active isolation. Setpoints for the bottom bucket and ribbons on the sidewall are received from the PC, after which

the internal controllers handle the heating control. Since the sensors on these heaters are not calibrated with high precision, an offset is required in these setpoints to achieve the correct wall temperature. The offset is determined by placing separate, calibrated sensors inside the isolation.

3.3.2 Measurements

Measurements are performed exclusively with the CompactRIO system, which is equipped with 4 regular ADCs, 4 PT100-specific ADCs and 36 ADCs for 3-wire resistance measurements.

The power dissipated in the bottom plate, and thus the power passing through the fluid to the top plate, is calculated from the voltage applied to the heater terminals and the current through a reference resistance of 0.10 Ω connected in series with the heaters, both measured with an ADC. A schematic view is shown in Figure 3-7. Due to the turbulent flow, the dissipated power fluctuates with approximately 0.5 W around the mean value at power fluxes below 50 W, increasing to 2.0 W variations for fluxes above 100 W, used for larger temperature differences in these experiments. The power is sampled 1.92 times per second.

In addition to the PT100-sensors in the copper plates, each plate contains four NTC thermistors at 0.7 mm from the copper-water interface, spaced equally at a radius of 100 mm. By connecting these sensors to the ADCs, the temperature variation in the plates can be measured directly. Calibration was performed at Tempcontrol [31], with every sensor connected to its corresponding ADC and with calibration points at 15, 32, 48 and 65 °C. The deviations of the plate temperature are at most 2% of the imposed temperature difference for the bottom plate, and at most 4% for the top plate.

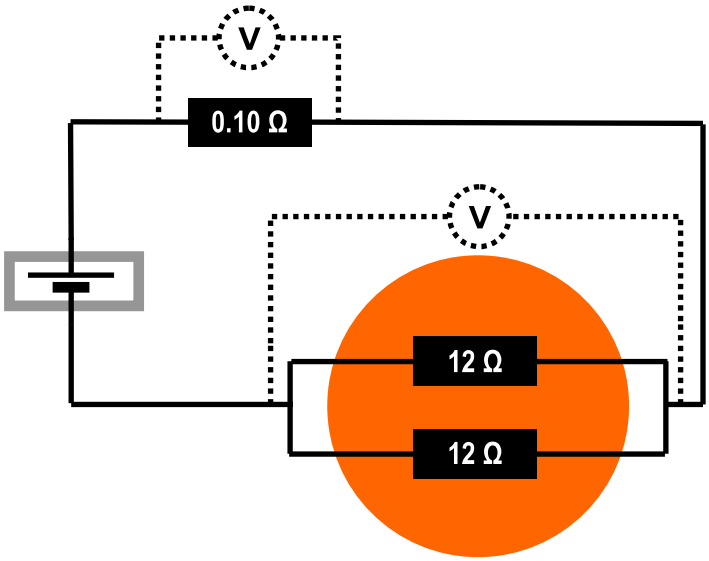

Figure 3-7: Schematic view of the electrical heating circuit, with two ADCs (depicted as potential meters) to calculate the dissipated power.

Next to sensors in the bottom and top plates, this experiment contains NTC thermistors in the sidewall as well, each connected to its own ADC. The sensors are placed very close (0.5 mm) to the water, so the direction of the LSC can be derived from the temperature profile. The Γ=1 sidewall contains three rows of eight equally spaced sensors, while the Γ=2 sidewall has one row of sixteen equally spaced sensors, both shown in Figure 3-8. Like the thermistors in the plates, these sensors are

calibrated at TempControl as well, resulting in an uncertainty of at most 0.001 K in the conversion from measured resistance to temperature. The sensors are wired in such a way to prevent large temperature gradients over the wire, thus eliminating heat flow through the copper wires to the sensor. All temperatures are sampled 1.00 times per second.

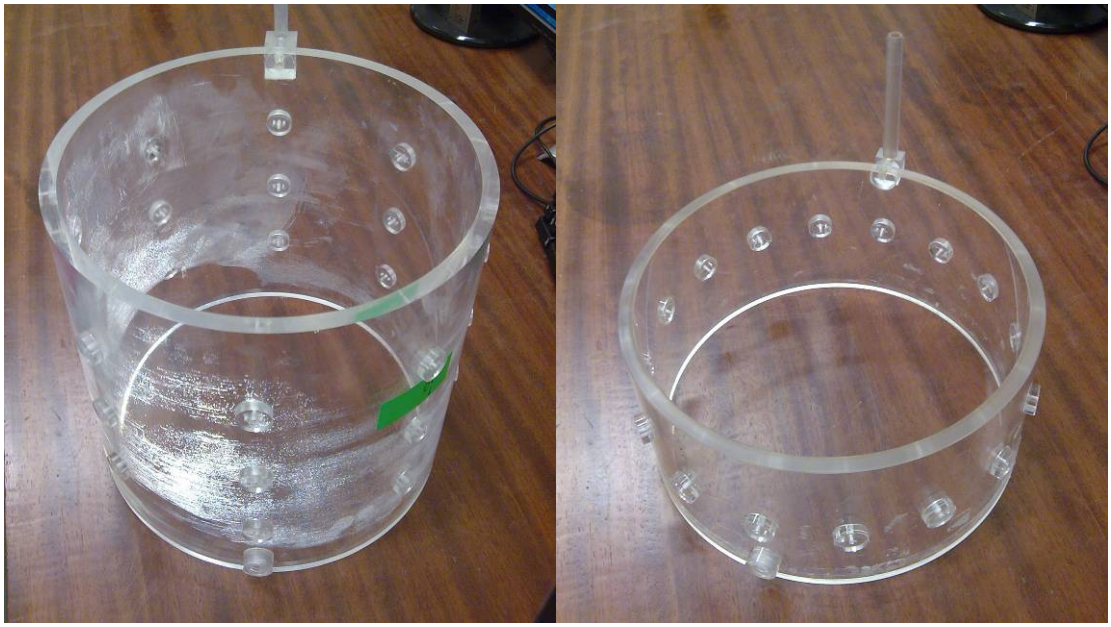

Figure 3-8: Left the Γ=1 sidewall with three rows of eight equally spaced sensor positions, right the Γ=2 sidewall with one row of sixteen equally spaced sensor positions, both without sensors and their wiring.

During preliminary tests of the setup it became clear that the way of measuring temperature with the CompactRIO influences the measurement itself. The ADCs measure the potential drop over the sensor at a current of approximately 300 μA. With this current, the sensors dissipate a substantial amount of heat and increase their own temperature. The problem is not very visible, since calibration usually compensates for this effect. However, the thermistors are placed in two materials with a very different heat conduction coefficient, so the sensors in the Plexiglas sidewall will be affected more by self-heating than the ones in the copper plates (0.10 K of self-heating compared to 0.04 K respectively). Since sensors in the same material are heated identically, those values can be compared without further issues. Comparing temperatures in the sidewall and the plates will results in significant errors, but those comparisons are not made in this experiment.

3.4 Data processing

The potentials and resistances measured by the CompactRIO system are sent to the LabView interface running on the PC, which converts them to power and temperature values using data from the calibration. The values are saved in separate files, one for the power and one for the 40 channels of temperature data. This results in roughly 28 MB of raw data for 24 hours of measurement. With this data, two different aspects are investigated: heat transport and LSC intensity

3.4.1 Heat transport

In section 2.1, the Rayleigh and Nusselt number were defined as

$$Ra = \frac{\beta g \Delta L^3}{\kappa \nu}, \tag{2.6}$$

$$Nu = \frac{QL}{\lambda \Delta}, \tag{2.8}$$

respectively. The fluid parameters are constant, but the temperature difference between the plates Δ and the height of the cell L are varied in the experiments, which leads to different values of the heat flux Q.
The average temperature of each plate is calculated from an area-weighted average of the five sensors present. The PT100 sensor, located at the centre of the plate, represents the inner section of the plate with a radius of 49 mm, while the four thermistors represent the four remaining sections, as shown in Figure 3-9. The two area-averaged temperatures are subtracted, resulting in the instantaneous temperature difference.

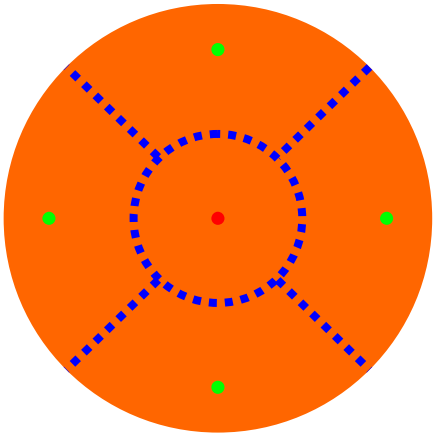

Figure 3-9: The PT100 (red) and the thermistors (green) with their weight areas outlined in blue.

The instantaneous heat flux is defined as

$$Q_i = \frac{P}{A} = \frac{P}{\pi R^2}, \tag{3.1}$$

with R the radius of the plate, so it can be calculated directly from the measured power P.
Since the Rayleigh-Bénard problem results in a turbulent flow, both the instantaneous temperature difference and the instantaneous heat flux will fluctuate over time. The first four hours of data are discarded, to make sure the system reached its final equilibrium state. The remaining data, which can range from six to over forty hours, is time-averaged to get the average value for the temperature difference Δ and the heat flux Q. In addition, the time-average is calculated for the last three-quarters and the last half of the remaining measurement time. The maximum difference between these values and the average value is used as the uncertainty in the average values. The calculations are illustrated in Figure 3-10.

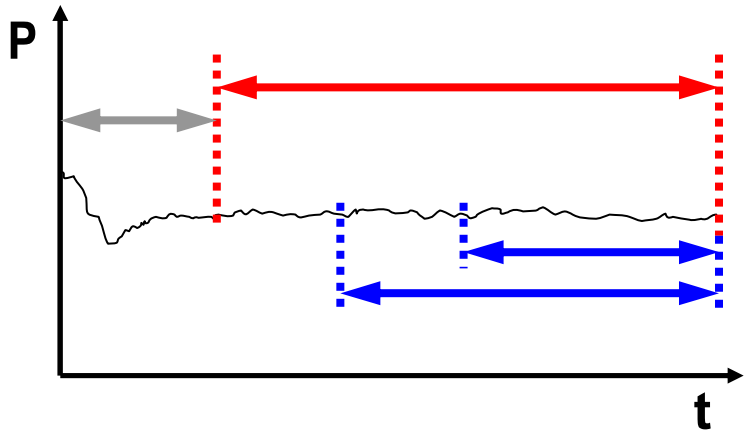

Figure 3-10: Illustration of the calculation of time-average values. The first four hours of the measurement (grey) are discarded. The average is calculated over the remaining interval (red), the uncertainty is determined from the maximum difference of average of two sub-intervals (blue) compared to the average of the whole interval (red).

Now that the temperature difference Δ, the heat flux Q and their respective uncertainties $\Delta\Delta$ and ΔQ are known, the Rayleigh number Ra and Nusselt number Nu can be calculated using (2.4) and (2.6) and their uncertainties with respectively

$$\Delta Ra = \left|\frac{\beta g L^3}{\kappa\nu}\right|\Delta\Delta\,, \tag{3.2}$$

$$\Delta Nu = \left|\frac{L}{\lambda\Delta}\right|\Delta Q + \left|-\frac{QL}{\lambda\Delta^2}\right|\Delta\Delta\,. \tag{3.3}$$

From previous theoretical research [14] it is predicted that the relation between the Nusselt number and the Rayleigh number can be approximated by a single power law, specifically

$$Nu \propto Ra^{1/3}\,. \tag{3.4}$$

Therefore, plots are made of the reduced Nusselt number defined as

$$Nu_{red} = \frac{Nu}{Ra^{1/3}}\,. \tag{3.5}$$

Experiments indicate that the exponent is approximately 0.3, but 1/3 remains customary. As explained in section 2.2, modest rotation can enhance heat transport. To investigate this effect, the heat transport fraction is calculated with

$$f = \frac{Nu(\Omega)}{Nu(\Omega = 0)}, \tag{3.6}$$

where the Rayleigh numbers of the static and rotating experiments should match. Since the temperature difference can show minute variations, linear interpolation is used on the static Nusselt number, to make sure the calculated fraction is correct. Since the setup is well able to achieve approximately the same temperature difference, the interpolation changes the Nusselt number by no more than 0.2% in these experiments. This fraction then is plotted as a function of the Rossby number.

3.4.2 Large-scale circulation

The sensors in the sidewall provide temperature information about the fluid close to the sidewall. If the single-cell LSC is the dominant flow mode, relatively hot fluid will flow up on one side and relatively cold fluid will flow down on the other side of the cell. The sensors in the sidewall will then register a sinusoidal temperature profile, of which the rising and descending sides of the LSC can be determined.

As with the heat transport measurement, the first four hours of data are discarded, to make sure the flow reached its equilibrium state. The sensor data is corrected for deviations between sensors by subtracting the signal at zero temperature difference from it. The temperature data for every ring is extracted and processed independently. For the Γ=1 experiment, there are three rings with eight sensors, while the Γ=2 experiment has one ring with 16 sensors. The data for a single ring at a single sample time is Fourier transformed. The amplitude of the LSC is calculated from the real part of the first sine mode, while the orientation is determined from the angle between the real and the imaginary part of that mode. A typical result of this method is shown in Figure 3-11.

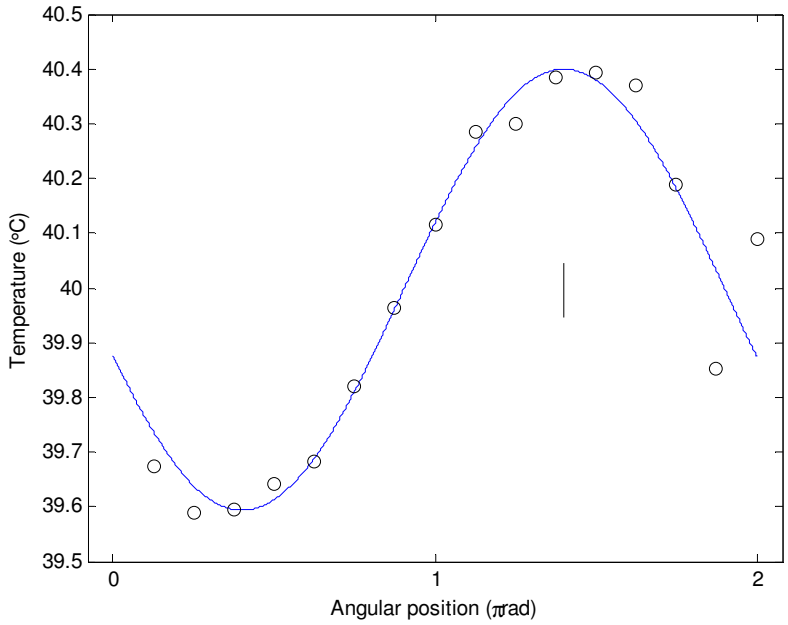

Figure 3-11: A typical view of the instantaneous sensor data (black circles) and the LSC profile resulting from Fourier analysis of this data (blue line) for a Γ=2 experiment. The black line indicates the angular position of the maximum temperature of the LSC.

This analysis is performed for every sample of the remaining data, resulting in the amplitude and the direction of the LSC as a function of time.

In addition to the sinusoidal LSC mode, the Fourier transform also provides information about higher modes. By normalizing and comparing the energies of different modes, the dominance of the LSC over higher modes can be investigated as a function of the rotation rate.

3.5 Measurement plan

Accurate investigation of the flow behaviour requires systematic variation of certain parameters. In all cases, the mean temperature of the fluid is 40 °C, making the Prandtl number 4.38. First, the heat flux under static conditions for the Γ=1 cell has to

be measured as a function of the temperature difference between the plates, to determine the Nusselt number as a function of the Rayleigh number. Second, the setup is rotated at different rotation rates at three different Rayleigh numbers, so the heat flux increase can be calculated as a function of the Rossby number. The maximum heat increase is expected around a Rossby number of 0.2 [20]. Third, these measurements are to be performed for the Γ=2 cell as well, at the same Rayleigh and Rossby numbers.

Due to material and sensory limitations, the range of temperature differences resulting in accurate measurements is limited. For the Γ=1 cell, the lowest temperature difference still producing acceptable results is 0.50 K, while temperature differences above 12.00 K suffer from isolation problems. The Γ=2 cell supports a temperature range from 1.00 K up to 20.00 K due to similar problems. An overview of the Rayleigh numbers achievable with these setups is shown in Figure 3-12.

Since the Rayleigh numbers need to be equal when performing rotating measurements, care has to be taken when picking measurement parameters. The Rayleigh numbers chosen for the rotating experiments are $2.99 \cdot 10^8$, $5.88 \cdot 10^8$ and $1.16 \cdot 10^9$. In addition, the Rossby numbers should preferably be similar for both cells, allowing for direct comparison of the heat flux increase. The Rotating Table Facility can provide rotation rates up to 10.0 rad/s, but these experiments require no more than 4.0 rad/s to detect a maximum in the heat flux increase. The lowest rotation rate is chosen 0.010 rad/s, to make sure the RTF is accurate in its applied rotation rate. Since the maximum heat transfer increase is of interest, more measurements will be performed in the lower Rossby number region. An overview of the Rossby numbers resulting from the rotation rates chosen for these experiments is shown in Figure 3-13.

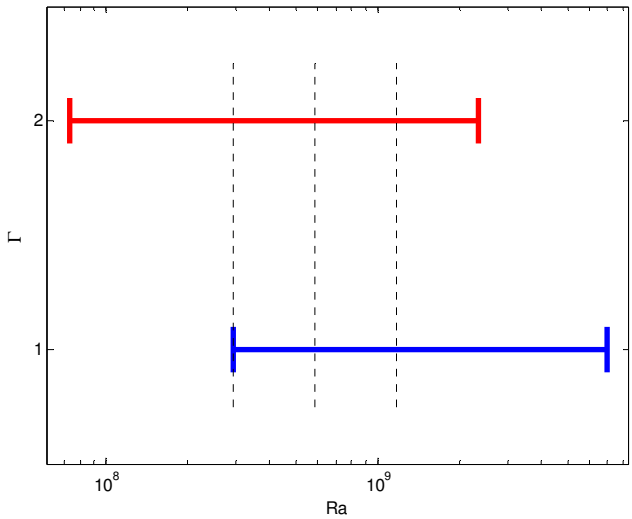

Figure 3-12: Possible Rayleigh number ranges for static experiments for the Γ=1 cell (blue) and the Γ=2 cell (red). The dashed lines represent the Rayleigh numbers chosen for the rotating experiments.

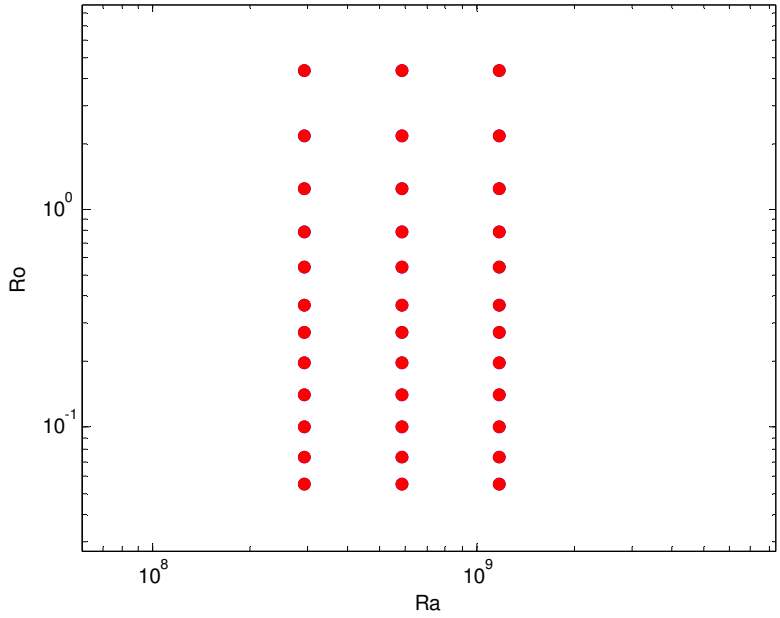

Figure 3-13: Rossby numbers at which the experiments are to be performed, for three different Rayleigh numbers for the Γ=1 cell and the Γ=2 cell (red).

With these measurement points, the Froude number (2.12) is always smaller than 0.01 for the Γ=1 experiments. For Γ=2 experiments, a higher rotation rate is required to achieve the same Rossby number, resulting in a larger Froude number. For Rossby numbers down to 0.2, the Froude number is well below 0.05, but for lower Rossby numbers it quickly increases up to as much as 0.52 for the largest Rayleigh number. At these low Rossby numbers, it is highly improbable that the centrifugal force is negligible, so care will have to be taken when analyzing and using the results of those measurements. It should be possible to detect a maximum in the heat transport, as a function of both the Rayleigh number and the aspect ratio, even without the troublesome low Rossby number measurements. The rotation rates for the two aspect ratios at the three chosen Rayleigh numbers are shown in Table 1.

Table 1: Rotation rates in radians per second for the two experimental setups at the three chosen Rayleigh numbers.

	AR 1.00			AR2.00		
Ra =	2.92e8	5.84e8	1.17e9	2.92e8	5.84e8	1.17e9
Ω =	0.010	0.014	0.020	0.040	0.057	0.080
	0.020	0.028	0.040	0.080	0.113	0.160
	0.035	0.049	0.070	0.140	0.198	0.280
	0.055	0.078	0.110	0.220	0.311	0.440
	0.080	0.113	0.160	0.320	0.453	0.640
	0.120	0.170	0.240	0.480	0.679	0.960
	0.160	0.226	0.320	0.640	0.905	1.280
	0.220	0.311	0.440	0.880	1.245	1.760
	0.310	0.438	0.620	1.240	1.754	2.480
	0.430	0.608	0.860	1.720	2.432	3.440
	0.600	0.849	1.200	2.400	3.394	4.800
	0.800	1.131	1.600	3.200	4.525	6.400

Chapter 4: Results

The measurement plan described in section 3.5 is performed with the experimental setup. The results from static and rotating heat transport measurements will be discussed first for both the Γ=1 and Γ=2 cell, followed by an analysis of the LSC in both static and rotating experiments.

4.1 Heat transport

The heat transport from the warmer bottom plate through the fluid to the cooler top plate is measured over a range of temperature differences and rotation rates. The results are compared with experimental data from other setups. First the results from static experiments will be presented, followed by the rotating experiments for the Γ=1 setup and for the Γ=2 setup.

4.1.1 Static experiments

The static experiments were performed both on the RTF and in a different room. The agreement between these two measurements sets is excellent, indicating the setup is not vulnerable to changes in its environment. A single measurement point is produced from 12 to 24 hours of raw data, as described in section 3.4.1. The results for Γ=1 and Γ=2 measurements are shown in Figure 4-1. Data from experiments in Santa Barbara are plotted for comparison [14].

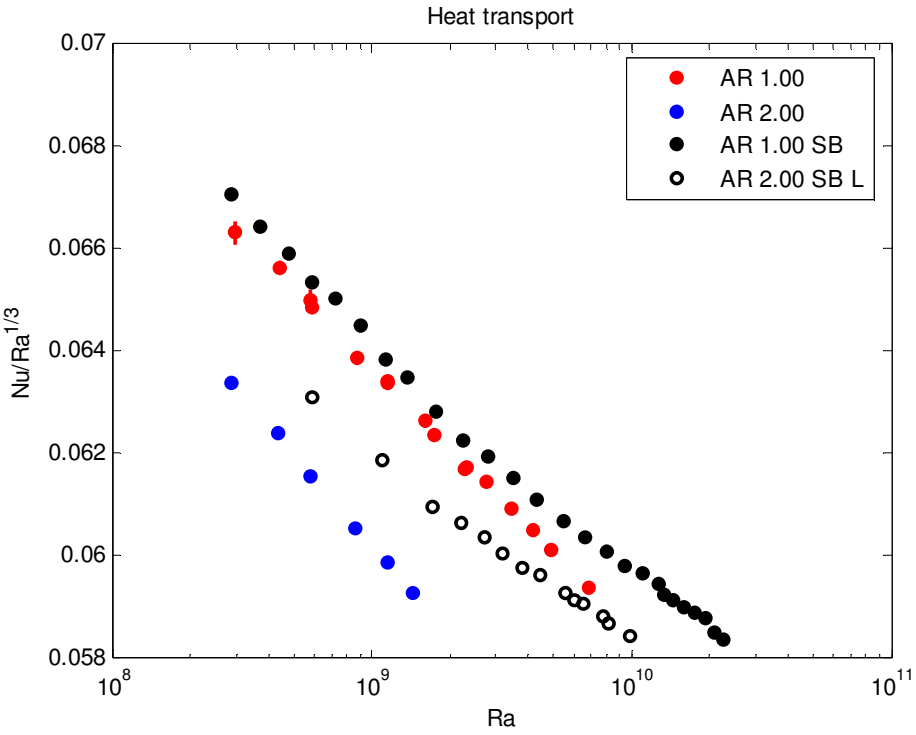

Figure 4-1: Reduced Nusselt number as a function of the Rayleigh number for the Γ=1 setup (red dots), the Γ=2 set=up (blue dots), and for a similar Γ=1 setup (black dots) and a larger Γ=2 setup (black circles) in Santa Barbara [14].

Within the range of Rayleigh numbers used for the rotating measurements (*Ra* from $3.0 \cdot 10^8$ to $2 \cdot 10^9$), the slope of the experimental data for Γ=1 is identical to the slope of the Γ=1 setup in Santa Barbara. The offset in the data is only minimal, approximately 1% of the value, making the agreement very good. The error bars are plotted, but are smaller than the plot symbol in most cases.

For Rayleigh numbers of $3 \cdot 10^9$ and higher, the current experimental data does not show a curvature like the data from the experiments in Santa Barbara, but remains a straight line. The origin of this difference is suspected to be related to the different methods used to actively isolate the sidewall in the experiments. The current setup uses a constant wall temperature, resulting in a sharp temperature difference at the junction of the sidewall and the bottom isolating bucket (see Figure 3-3), which may heat fluid via the sidewall. A thorough analysis of both setups might reveal the optimal method, but is hardly relevant for the current rotating experiments.

The Γ=2 experimental data shows a slightly different slope, but more noticeably an offset of about 6% compared to Γ=1 data. Experiments in Santa Barbara showed a difference between the two aspect ratios as well, though the difference was smaller in that case. It is likely that the shape of the LSC is more elliptical in the Γ=2 experiments than in the Γ=1 case. This could decrease the speed at which the fluid moves in the LSC, lowering its ability to generate heat-transporting plumes and thus resulting in a lower Nusselt number. Numerical simulations or in situ PIV measurements are required to form a definitive conclusion on this aspect.

The measurement data can be found in Appendix A.1.

4.1.2 Rotating experiments

All rotating experiments are performed on the RTF, under the same conditions as the static experiments on the RTF. All data points come from measurements with duration

of 12 hours, making it possible to cover the entire range of Rayleigh and Rossby numbers for a single aspect ratio within three weeks. The results for the Γ=1 setup are shown in Figure 4-2, with data from experiments in Santa Barbara for comparison [19]. The heat transport fraction for the Γ=2 setup is shown in Figure 4-3, and the absolute Nusselt number for the measurements is plotted in Figure 4-4.

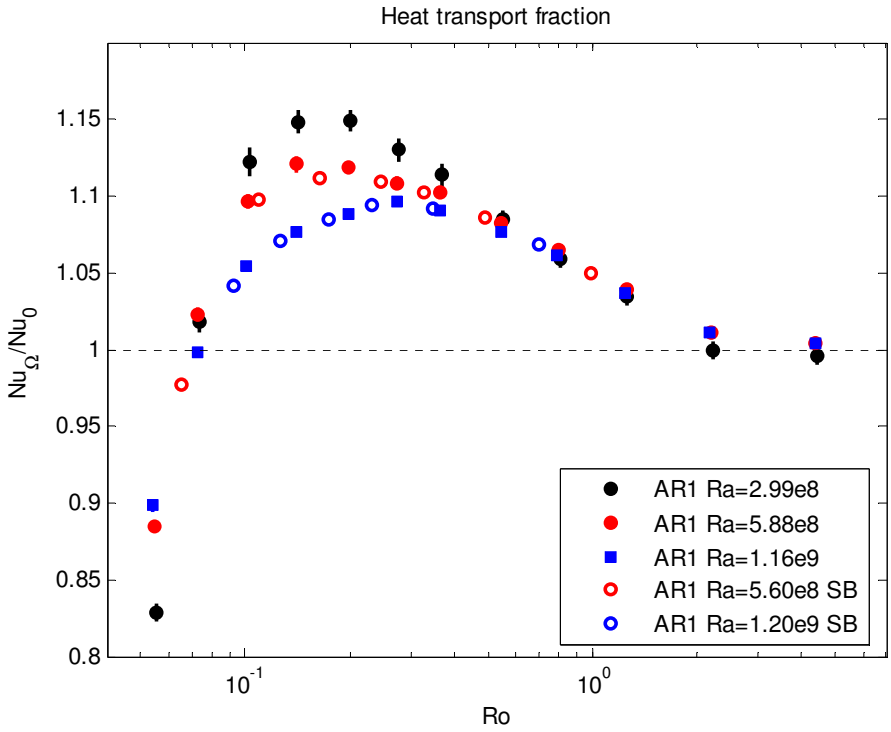

Figure 4-2: Heat transport fraction as a function of the Rossby number for the Γ=1 setup at Rayleigh numbers of $2.99 \cdot 10^8$ (black dots), $5.88 \cdot 10^8$ (red dots) and $1.16 \cdot 10^9$ (blue dots) and for a similar Γ=1 setup in Santa Barbara at $5.60 \cdot 10^8$ (red circles) and $1.20 \cdot 10^9$ (blue circles) [19].

As expected, modest rotation enhances heat transport with up to 15% for the Γ=1 setup, depending on the Rayleigh number. For Rossby numbers of approximately 2 and lower, heat transport gradually increases to a maximum. Higher Rayleigh numbers show a smaller enhancement, and the maximum heat transfer occurs at a higher Rossby numbers. For all Rayleigh numbers, the heat transfer quickly drops again at even lower Rossby numbers due to suppression of vertical velocity fluctuations by the Taylor-Proudman theorem (see section 2.2) [20][25]. At lower Rayleigh numbers, the drop in heat transport fraction is more pronounced than at higher ones. All results match very well with data from similar experiments in Santa Barbara.

One peculiarity is the difference between $Ra=2.99 \cdot 10^8$ and the other two experiments. The transition from the static state to the rotation-enhanced state seems to be sharper and at a slightly lower Rossby numbers compared to experiments at the two higher Rayleigh numbers. This may be caused by the low temperature difference between the top and bottom plate, slightly preventing the formation of LSC-breaking tubes and thus postponing the rotational enhancement.

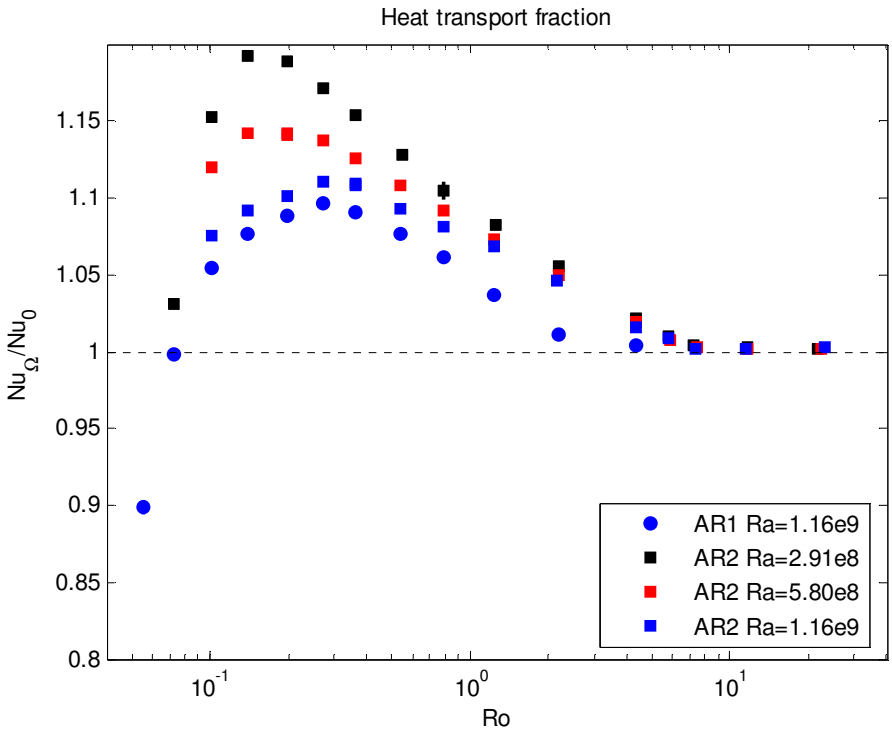

Figure 4-3: Heat transport fraction as a function of the Rossby number for the Γ=2 setup at Rayleigh numbers of $2.91 \cdot 10^8$ (black squares), $5.80 \cdot 10^8$ (red squares) and $1.16 \cdot 10^9$ (blue squares), and for the Γ=1 setup at a Rayleigh number of $1.16 \cdot 10^9$ (blue dots).

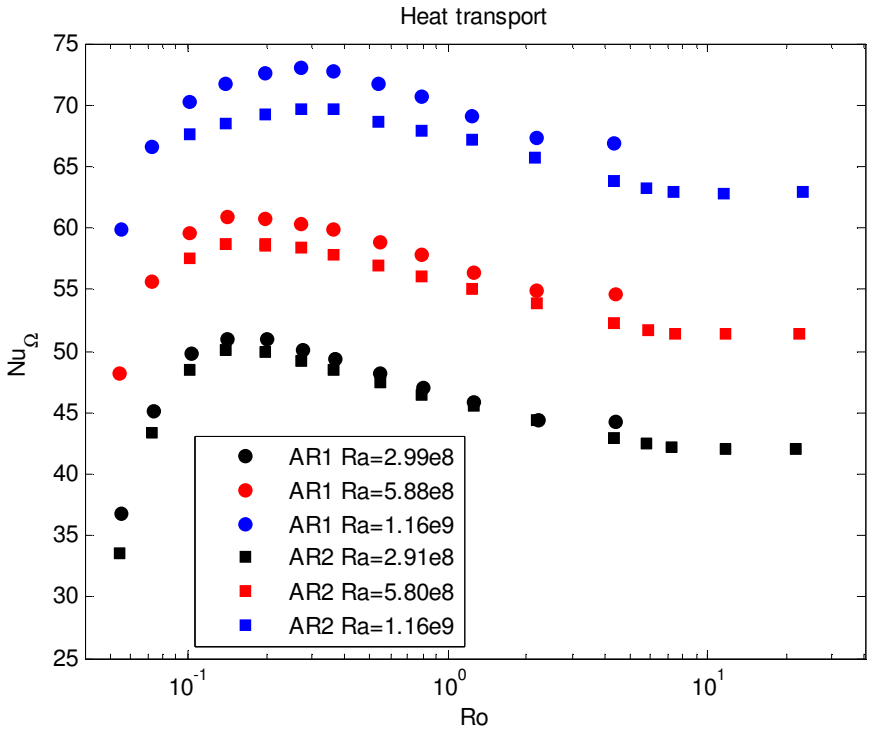

Figure 4-4: Absolute Nusselt number as a function of the Rossby number for the Γ=1 setup at Rayleigh numbers of $2.99 \cdot 10^8$ (black dots), $5.88 \cdot 10^8$ (red dots) and $1.16 \cdot 10^9$ (blue dots) and for the Γ=2 setup at Rayleigh numbers of $2.91 \cdot 10^8$ (black squares), $5.80 \cdot 10^8$ (red squares) and $1.16 \cdot 10^9$ (blue squares)

The results from the Γ=2 experiments show the same general behaviour. Starting from a Rossby number of roughly 7, the heat transport increases to a maximum of an additional 20% compared to the static case, after which it drops again. The maximum

in the heat transport occurs at approximately the same Rossby number for both setups. Unfortunately, hardware communication issues made it impossible to perform accurate measurements with the Γ=2 setup at the lowest Rossby numbers for the two higher Rayleigh numbers.
There are some striking differences between the results from the Γ=1 and Γ=2 experiments. For Γ=2, the absolute Nusselt number is slightly lower, even for low Rossby numbers, as can be seen in Figure 4-4. This deviation is larger for higher Rayleigh numbers. Heat transport through Ekman pumping was expected to result in the same absolute Nusselt numbers, since heat transport is essentially boundary layer dominated in that case. However, these measurements indicate a significant dependence on the aspect ratio and a slight dependence on the Rayleigh number. Further research is required to provide a solid explanation for these results.
Another interesting and more notable difference between the two setups is the onset of the heat transport increase. Four additional measurements have been performed at each Rayleigh number, to capture the exact position of the onset. While for Γ=1 the heat transport started increasing at a Rossby number of 2, the onset is located roughly at a Rossby number of 7 for Γ=2. Investigation of the data shows the onset is located at a slightly higher rotation rate than for Γ=1, indicating that this effect is not purely based on the boundary layer. Note that the additional measurements on this onset are shorter than the rest of the measurement points, which slightly increases the uncertainty in the data points.
The position of the onset is determined by the equilibrium between the LSC and Ekman pumping. When the rotating rate increases, the strength of Ekman pumping increases as well, allowing the tubes to destroy the LSC and increase heat transport. The lower Nusselt number in the non-rotating case indicates the LSC is less intense in a static Γ=2 setup than in the Γ=1 case, allowing the Ekman pumping to destroy it at a higher Rossby number.
The measurement data can be found in Appendix A.2.

4.2 Large-scale circulation

The orientation and intensity of the LSC and higher modes can be determined from the temperature sensors located on the sidewall, as described in section 3.4.2. The intensity of the LSC as a function of the rotation rate will be discussed first, followed by a brief analysis of the preferential orientation of the LSC in the current setup.

4.2.1 LSC intensity

For all static measurements with a non-zero temperature difference between the plates, the single-cell mode of the LSC is by far the strongest mode present in the flow, as can be seen in Figure 4-5. Other modes are a factor 3 to 10 weaker.

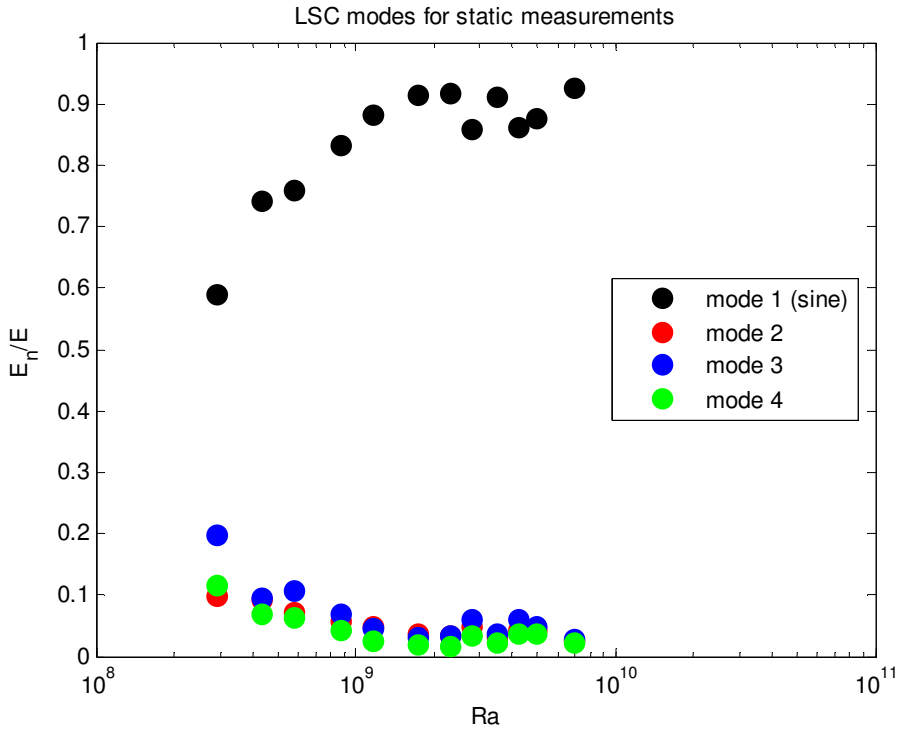

Figure 4-5: Normalized Fourier mode energy as a function of the Rayleigh number for the Γ=1 setup. The graph shows the intensity of the single-cell mode (black) and higher modes (red, blue and green).

For the rotating experiment with the Γ=1 setup at a Rayleigh number of $1.16 \cdot 10^9$, the mode intensity is shown in Figure 4-6. From previous numerical research, the LSC is expected to start disappearing for Rossby numbers lower than 2.5 [22].

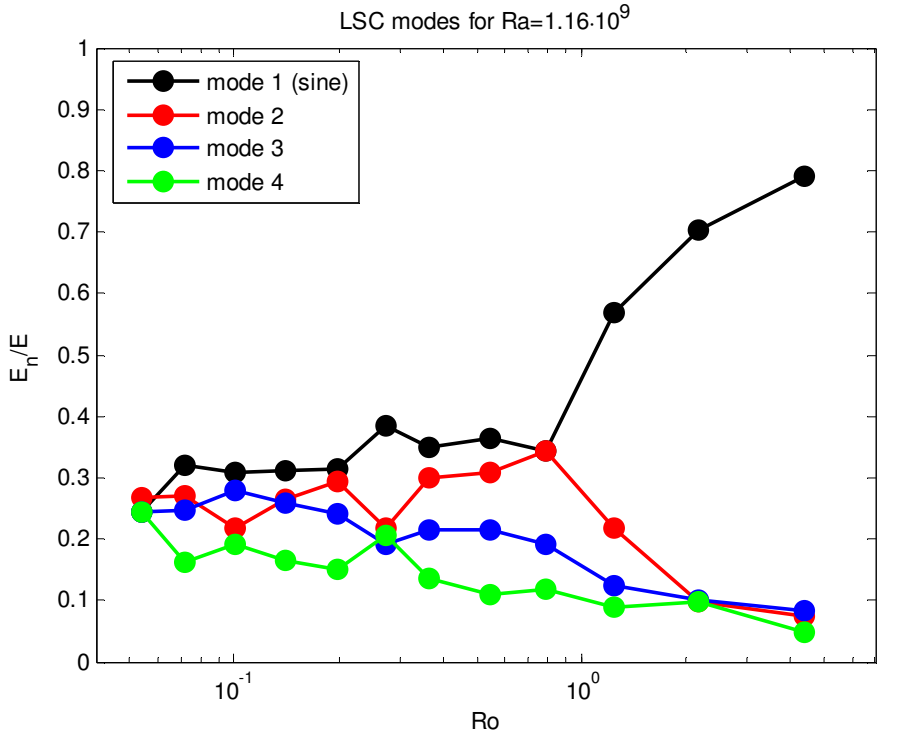

Figure 4-6: Normalized Fourier mode energy as a function of the Rossby number for a Rayleigh number of $1.16 \cdot 10^9$ for the Γ=1 setup. Shown are the single-cell mode (black) and higher modes (red, blue and green).

For high Rossby numbers, which correspond with none to low rotation, the single-cell circulation is the dominant mode. With Rossby numbers lower than 2, the intensity of the single-cell mode drops and that of the second mode rises, showing that the single-cell LSC is partly destroyed by modest rotation as expected. These experimental results agree very well with earlier numerical work [22]. For even lower Rossby numbers (*Ro*<0.5), thus at high rotation rates, the single-cell mode is expected to disappear to the noise level of 0.25, since vertical tubes should dominate the flow. The strength of the single-cell mode decreases considerably, but it remains present even at the lower Rossby numbers. This is probably due to the setup not being a truly ideal system, which will be described in more detail in section 4.2.2.

The disappearance of the single-cell mode coincides with the increase in heat transport. The heat transport starts to increase when the single-cell mode has a normalized intensity of 0.7, but continues to increase well after the single-cell mode has reached its final low intensity. This again shows that the increase in heat transport is caused by a different mechanism than the LSC.

The Γ=2 setup has more sensors in the sidewall, making it possible to detect higher modes in the temperature profile and making measurements less vulnerable to single-sensor variations. As with the Γ=1 setup, the single-cell mode is the strongest mode present in static experiments. The mode intensity for rotating experiments at a Rayleigh number of $1.16 \cdot 10^9$ is shown in Figure 4-7. With 16 sensors on the sidewall, the Γ=2 setup can detect higher modes (up to mode 8) and has a lower noise level (0.125).

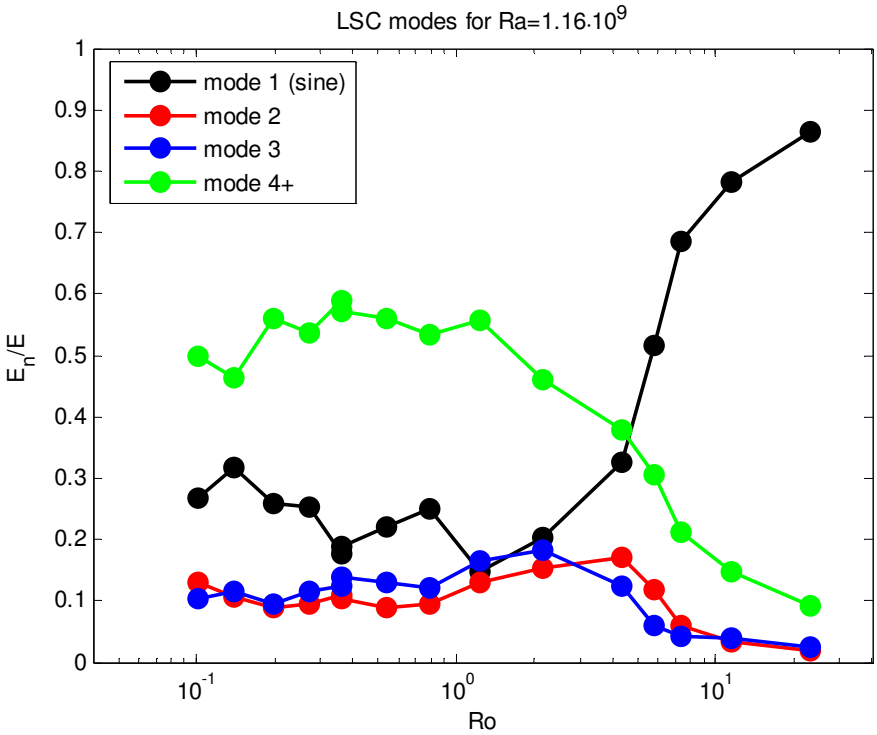

Figure 4-7: Normalized Fourier mode energy as a function of the Rossby numbers for a Rayleigh number of $1.16 \cdot 10^9$ for the Γ=2 setup. Shown are the single-cell mode (black), mode 2 (red), mode 3 (blue) and the sum of mode 4 and higher (green).

As with Γ=1, the single-cell mode is dominant for high Rossby numbers. The intensity of the single-cell mode makes a large drop when the Rossby number is decreased form 7 to 4, so modest rotation destroys the single-cell LSC. Compared to the Γ=1 experiments, this destruction occurs at a higher Rossby number in the Γ=2

setup, which was expected considering the position of the onset of the heat transport increase (section 4.1.2). Again, heat transport starts increasing once the single-cell mode intensity reaches 0.7, and continues to increase well beyond the disappearance of the single-cell mode. At the same Rayleigh number, the transition is a lot sharper than with Γ=1, which indicates the Rayleigh number is not the only important parameter in this case.
At high rotation rates, the single-cell mode is still present in Γ=2 experiments, and its normalized mode energy even increases. The increase is largely caused by the decreasing absolute intensity of the higher modes, while the single-cell mode intensity remains approximately constant.

4.2.2 LSC orientation preference

The orientation of the LSC can be defined by the angular position of the maximum temperature of the sine fit explained in section 3.4.2. Based on cylindrical symmetry, the LSC is expected not to have a preferential orientation, but experiments proved the contrary. During static experiments with the Γ=1 setup and the Γ=2 setup, the single-cell LSC tends to be 'locked' in a fixed direction, irrespective of activity of the isolation heaters and nearly independent of the temperature difference between the top and bottom plates. This effect has been described before and seems to be stronger for larger aspect ratios [17]. A probability density function of the LSC direction is created from the static measurements performed for section 4.1.1. The probability density function of the LSC angle is wider for the Γ=1 setup, as shown in Figure 4-8, which confirms the weaker 'locking' in smaller aspect ratios. Still, there are orientations, both for Γ=1 and for Γ=2, which the LSC will avoid.

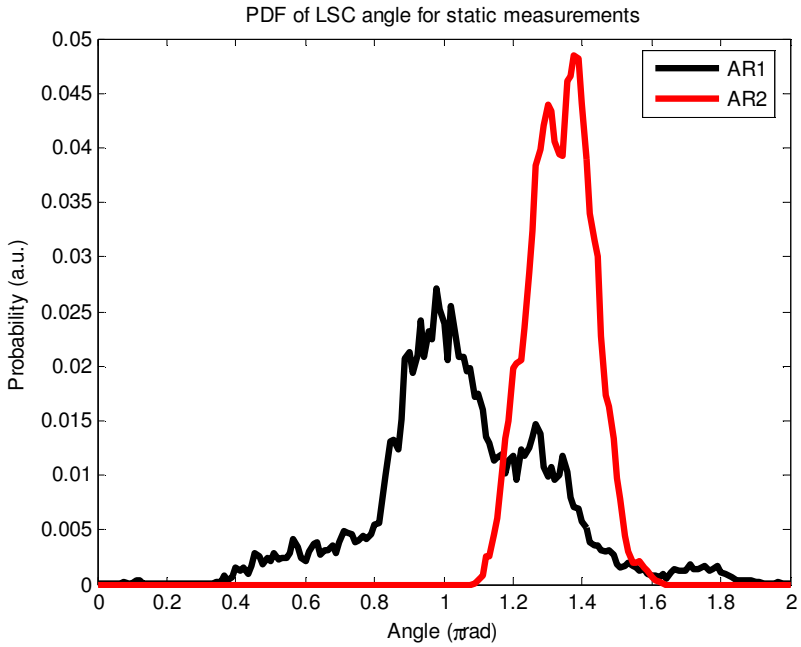

Figure 4-8: Probability density function of the LSC angle for the Γ=1 (black) and Γ=2 (red) setups. Data from 70 hours of static experiments (section 4.1.1) is used in both cases, with Rayleigh numbers from the overlapping region only (see section 3.5).

By performing static experiments on the RTF under different angles between the convection cell and the laboratory, the origin of the preferential orientation can be estimated. The orientation of the LSC in those static experiments is plotted in Figure 4-9 in the co-rotated convection cell frame.

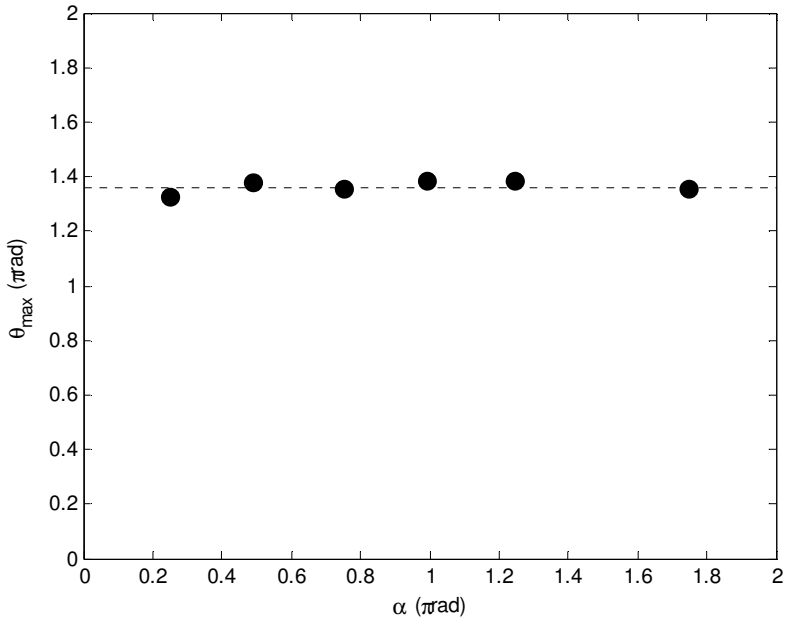

Figure 4-9: LSC direction in the convection cell frame θ_{max} (dots) as a function of the rotation angle α of the Γ=2 experiment, with the average value (dashed line)

Clearly, the LSC is oriented in the same direction in the convection cell in all cases, irrespective of the angle between the setup and the laboratory, eliminating any external effects. The angular position of the warm side of the LSC is directly opposite to the top plate's cold spot, which is generated at the inflow position of coolant. It can be concluded that small temperature non-uniformities in the top and bottom boundaries can dominate the LSC orientation to a great extent. Unfortunately, it is not possible to eliminate this non-uniformity with the current setup, as it arises from the cooling method used.

It should be noted that the orientation of the LSC hardly has any impact on the heat transport, as the difference in Nusselt number is less than 0.5% when the LSC is forced in a different orientation.

Chapter 5: Conclusion

Turbulent thermal convection has been investigated experimentally in a rotating Rayleigh-Bénard system. Experimental setups with aspect ratios Γ of 1 and 2 have been constructed to measure the heat transport and flow structure in water at a Prandtl number of 4.38, with Rayleigh numbers between $2 \cdot 10^8$ and $2 \cdot 10^9$ and Rossby numbers ranging from 0.1 to 10.

For Γ=1, non-rotating measurements resulted in Nusselt numbers in very good agreement with previous research by other groups, with only minor deviations outside of the operational range. Static measurements for Γ=2 resulted in Nusselt numbers 6% lower than the Γ=1 data, which probably indicates a more elliptical shape and lower flow speed of the LSC.
Adding rotation to the system introduces a transition, whereby rotation can enhance heat transport between the hot and cold boundary. In experiments at modest rotation rates, the Nusselt number increased up to 15% for Γ=1, and up to 20% for Γ=2. As lower Rayleigh numbers show a larger enhancement, even larger increases are possible at lower Rayleigh numbers. The results for Γ=1 agree very well with previous experimental data. There is a slight difference between the absolute Nusselt numbers of the two aspect ratios which requires an explanation.
A major difference between the two aspect ratios is the position of the onset of rotational enhancement. The Rossby number at which heat transport starts to increase is independent of the Rayleigh number, but shifts from Ro=2 to Ro=7 when going from Γ=1 to Γ=2. The Ekman pumping responsible for the heat transport increase is able to overcome the weaker LSC in Γ=2 at a higher Rossby number, thus shifting the onset. It would be interesting to investigate this shift in intermediate and larger aspect ratios, and especially if the LSC consists of two rolls, rather than the current single-roll shape.
In addition to the heat transport between the boundaries, the temperature profile on the sidewall is registered to extract flow patterns from. In static experiments, the single-roll configuration of the LSC is by far the dominant mode, both for Γ=1 and Γ=2. When reaching a sufficiently low Rossby number, the strength of this single-cell mode will start to decrease, where the transition in Γ=2 is sharper than in Γ=1. The disappearance of the single-cell mode roughly coincides with the onset of rotational heat transfer enhancement in both aspect ratios, which corresponds with the assumption that heat transport is taken over from the LSC by Ekman pumping.
Static measurements with both aspect ratios showed that the direction of the LSC, defined as the angular position of its warm side, has a pronounced preference for a

certain position. For Γ=2, the direction of the LSC is more concentrated around a single preferential position than for Γ=1, which confirms more intense locking in higher aspect ratios. This locking of the LSC is the result of a temperature non-uniformity in the cold boundary, specifically a cold spot caused by the inflow of coolant. Since this experimental issue hampers the possibility of the LSC to change its orientation, attempts should be made prevent this cold spot.

In summary, rotational heat transport enhancement is investigated in Rayleigh-Bénard convection with aspect ratios one and two. The results for Γ=1 agree with previous research. The results for rotating Γ=2 are the first in this field and show that the rotational transition has a remarkable dependence on the aspect ratio. The profile of the LSC is extracted from temperature data, and shows that the single-cell mode is indeed destroyed when Ekman pumping takes over heat transport.

5.1 Acknowledgements

The experiments described in this report are part of the promotion project of Richard Stevens, which will contain experimental results for an additional, intermediate aspect ratio and numerical results on all aspect ratios as well. I would like to thank him for the guidance during this project, and I would like to thank Herman Clercx for the regular meetings with feedback and supervision.
The experimental work would not have been possible without the assistance and expertise of the technical staff at the Turbulence and Vortex Dynamics group of the Eindhoven University of Technology. Therefore, I would like to thank Ad Holten for his help with the RTF, Gerald Oerlemans for every mechanical aspect of the setup and for the precise drawings, and especially Freek van Uittert for the design of the electronics and control software and for the continuous support during the experiments.
Also, I would like to thank my fellow student Joris for the, occasionally fruitful, conversations during lunch breaks. I would also like to use this graduation project to thank my parents for their continuous investments in my education over the past years. Finally, I would like to thank Lieke, my girlfriend, for all the love and support she gives me every day.

References

[1] D. Hartmann, L. Moy and Q. Fu 2001 *Tropical convection and the energy balance at the top of the atmosphere*. Journal of Climate **14** 4495-4511

[2] T. Paluszkiewicz, R. Garwood and D. Denbo 1994 *Deep convective plumes in the ocean*. Oceanography **7-2** 37-44

[3] P. Cardin and P. Olson 1994 *Chaotic thermal convection in a rapidly rotating spherical shell: consequences for flow in the outer core*. Physics of the Earth and Planetary Interiors **82** 235-259

[4] F. Busse 1994 *Convection driven zonal flows and vortices in major planets*. Chaos **4-2** 123-134

[5] A. Sakuraba & P. Roberts 2009 *Generation of a strong magnetic field using uniform heat flux at the surface of the core*. Nature Geoscience **2-11** 802-805

[6] M. Dunn 2001 *Convective heat transfer and aerodynamics in axial flow turbines*. Journal of Turbomachinery **123** 637-686

[7] H. van Santen, C. Kleijn, H. van den Akker 2000 *On turbulent flows in cold-wall CVD reactors*. Journal of Crystal Growth **212** 299-310

[8] H. Bénard 1901 *Les tourbillons cellulaires dans une nappe liquide transportant de la chaleur par convection en régime permanent*. Annales de Chimie et de Physique **23** 62-144

[9] Lord Rayleigh 1916 *On convection currents in a horizontal layer of fluid, when the higher temperature in on the under side*. Philosophical Magazine **32** 529-546

[10] S. Chandrasekhar *Hydrodynamic and hydromagnetic stability.* Oxford University Press, Oxford (1961)

[11] H. Rossby 1969 *A study of Bénard convection with and without rotation*. Journal of Fluid Mechanics **36-2** 309-335

[12] X. Chavanne, F. Chillà, B. Chabaud, B. Castaing, J. Chaussy & B. Hébral 1996 *High Rayleigh number convection with gaseous helium at low temperature*. Journal of Low Temperature Physics **104-1** 109-129

[13] C. Sun, L. Ren, H. Song & K. Xia 2005 *Heat transport by turbulent Rayleigh-Bénard convection in 1 m diameter cylindrical cells of widely varying aspect ratio*. Journal of Fluid Mechanics **542** 165-174

[14] D. Funfschilling, E. Brown, A. Nikolaenko & G. Ahlers 2005 *Heat transport by turbulent Rayleigh-Bénard convection in cylindrical samples with aspect ratio one and larger*. Journal of Fluid Mechanics **536** 145-154.

[15] S. Grossman & D. Lohse 2001 *Thermal convection for large Prandtl number*s. Physical Review Letters **86** 15

[16] A. Ebert, C. Resagk & A. Thess 2008 *Experimental study of temperature distribution and local heat flux for turbulent Rayleigh-Bénard convection of air in a long rectangular enclosure*. International Journal of Heat and Mass Transfer **51** 4238-4248
[17] H. Xi & K. Xia 2008 *Azimuthal motion, reorientation, cessation and reversal of the large-scale circulation in turbulent thermal convection: a comparative study in aspect ratio one and one-half geometries*. Physical Review E **78** 036326
[18] R. Verzicco 2004 *Effect of nonperfect thermal sources in turbulent thermal convection*. Physics of Fluids **16** 1965
[19] E. Brown, A. Nikolaenko, D. Funfschilling & G. Ahlers 2005 *Heat transport in turbulent Rayleigh-Bénard convection: Effect of finite top- and bottom-plate conductivities*. Physics of Fluids **17** 075108
[20] J. Zhong, R. Stevens, H. Clercx, R. Verzicco, D. Lohse & G. Ahlers 2009 *Prandtl-, Rayleigh- and Rossby-number dependence of heat transport in turbulent rotating Rayleigh-Bénard convection*. Physical Review Letters **102** 044502
[21] R. Kunnen *Turbulent rotating convection*. PhD thesis, Eindhoven University of Technology, 2008
[22] R. Kunnen, H. Clercx & B. Geurts 2008 *Breakdown of large-scale circulation in turbulent rotating convection*. EPL **84** 24001
[23] R. Kunnen, B. Geurts & H. Clercx 2010 *Experimental and numerical investigation of turbulent convection in a rotating cylinder*. Journal of Fluid Mechanics **642** 445-476
[24] R. Stevens, J. Zhong, H. Clercx, G. Ahlers & D. Lohse 2009 *Transitions between turbulent states in rotating Rayleigh-Bénard convection*. Physical Review Letters **103** 024503
[25] R. Kunnen, H. Clercx, B. Geurts 2006 *Heat flux intensification by vortical flow localization in rotating convection*. Physical Review E **74** 056306
[26] G. Ahlers 2009 *Turbulent convection*. Physics **2** 74
[27] L. Kadanoff 2001 *Turbulent heat flow: structures and scaling*. Physics Today **54** 34-39
[28] H. Greenspan *The theory of rotating fluids*. Cambridge University Press, Cambridge (1968)
[29] J. Pedlosky *Geophysical fluid dynamics*. Springer, Berlin (1987)
[30] L. van Bokhoven, H. Clercx, G. van Heijst & R. Trieling *Experiments on rapidly rotating turbulent flows*. Physics of Fluids **21** 096601
[31] Tempcontrol Industrial Electronic Products B.V., van Alphenstraat 63S, Voorburg, www.tempcontrol.nl

Appendix A: Measurement data

This appendix contains the measurement data for all experiments with the Γ=1 and the Γ=2 cell. For the static experiments, the temperatures difference (in K) after area- and time-averaging (described in section 3.4.1) and the power (in W) after correction for heat leakage and time-averaging are given, followed by the dimensionless Rayleigh and Nusselt numbers resulting from them. For the rotating experiments, the rotation rate (in rad/s) and the power (in W) after correction for heat leakage and time-averaging are given, followed by the dimensionless Rossby number and the heat transport fraction (3.6). Note that all rotating experiments are performed on the RTF, but the static experiments only partly on the RTF and partly in a different lab for the Γ=1 setup..

A.1 Static experiments

AR 1.00 static (CC0.02)

Temperature		Power		Rayleigh	Nusselt	
0.99184 ±	0.00018	6.64635 ±	0.01918	5.79e+008 ± 1.08e+005	54.17141 ±	0.16642
1.97586 ±	0.00015	16.23277 ±	0.03535	1.15e+009 ± 8.61e+004	66.41507 ±	0.14960
2.77636 ±	0.00057	25.26378 ±	0.04266	1.62e+009 ± 3.34e+005	73.56179 ±	0.13938
3.93732 ±	0.00023	39.67892 ±	0.04861	2.30e+009 ± 1.33e+005	81.46838 ±	0.10452
4.73359 ±	0.00076	50.46666 ±	0.05940	2.76e+009 ± 4.46e+005	86.18732 ±	0.11534
5.89517 ±	0.00118	67.07850 ±	0.04508	3.44e+009 ± 6.91e+005	91.98483 ±	0.08028
7.12708 ±	0.00147	85.77530 ±	0.08574	4.16e+009 ± 8.57e+005	97.29269 ±	0.11729
8.32791 ±	0.00023	104.88233 ±	0.05641	4.86e+009 ± 1.33e+005	101.81126 ±	0.05753
11.72459 ±	0.00159	163.61891 ±	0.07693	6.85e+009 ± 9.28e+005	112.81460 ±	0.06833

AR 1.00 static (RTF)

Temperature		Power		Rayleigh	Nusselt	
0.51276 ±	0.00006	2.81303 ±	0.00928	2.99e+008 ± 3.25e+004	44.34932 ±	0.15110
0.75967 ±	0.00013	4.70625 ±	0.00777	4.44e+008 ± 7.52e+004	50.08177 ±	0.09121
1.00603 ±	0.00006	6.76150 ±	0.01153	5.88e+008 ± 3.46e+004	54.33302 ±	0.09581
1.49770 ±	0.00036	11.31847 ±	0.01850	8.75e+008 ± 2.09e+005	61.09318 ±	0.11443
1.98922 ±	0.00050	16.39436 ±	0.01077	1.16e+009 ± 2.92e+005	66.62558 ±	0.06055
2.96944 ±	0.00030	27.50332 ±	0.01955	1.73e+009 ± 1.77e+005	74.87566 ±	0.06086
3.94824 ±	0.00083	39.86758 ±	0.02360	2.31e+009 ± 4.85e+005	81.62931 ±	0.06550

AR2.00 static (RTF)

Temperature		Power		Rayleigh	Nusselt	
3.97534 ±	0.00005	41.26782 ±	0.00774	2.90e+008 ± 3.84e+003	41.96009 ±	0.00842
5.94738 ±	0.00058	69.50715 ±	0.01946	4.34e+008 ± 4.20e+004	47.23931 ±	0.01780
7.91525 ±	0.00016	100.39962 ±	0.02441	5.78e+008 ± 1.16e+004	51.27040 ±	0.01349
11.84863 ±	0.00059	169.05056 ±	0.01898	8.65e+008 ± 4.31e+004	57.66973 ±	0.00935
15.77402 ±	0.00075	244.86585 ±	0.05520	1.15e+009 ± 5.44e+004	62.74591 ±	0.01711
19.68607 ±	0.00132	325.75584 ±	0.08107	1.44e+009 ± 9.64e+004	66.88560 ±	0.02113

A.2 Rotating experiments

AR 1.00 rotating – DT = 0.51 K – Ra = $2.99 \cdot 10^8$

Rotation rate		Power		Rossby		fraction	
0.01000 ±	0.00005	2.79943 ±	0.00727	4.41633 ±	0.02226	0.99610 ±	0.00603
0.02000 ±	0.00010	2.80649 ±	0.00642	2.20760 ±	0.01133	0.99933 ±	0.00612
0.03500 ±	0.00018	2.90569 ±	0.00680	1.26171 ±	0.00651	1.03414 ±	0.00589
0.05500 ±	0.00028	2.97480 ±	0.00539	0.80278 ±	0.00416	1.05918 ±	0.00582
0.08000 ±	0.00040	3.04989 ±	0.00458	0.55203 ±	0.00278	1.08528 ±	0.00541
0.12000 ±	0.00060	3.13023 ±	0.00830	0.36806 ±	0.00189	1.11355 ±	0.00722
0.16000 ±	0.00080	3.17520 ±	0.01111	0.27600 ±	0.00139	1.13008 ±	0.00783
0.22000 ±	0.00110	3.23092 ±	0.00677	0.20076 ±	0.00102	1.14931 ±	0.00664
0.31000 ±	0.00155	3.22797 ±	0.00816	0.14248 ±	0.00074	1.14814 ±	0.00767
0.43000 ±	0.00215	3.15396 ±	0.01430	0.10270 ±	0.00053	1.12234 ±	0.00964
0.60000 ±	0.00300	2.86138 ±	0.00743	0.07361 ±	0.00037	1.01799 ±	0.00634
0.80000 ±	0.00400	2.33111 ±	0.00786	0.05524 ±	0.00028	0.82813 ±	0.00588

AR 1.00 rotating – DT = 1.00 K – Ra = $5.88 \cdot 10^8$

Rotation rate		Power		Rossby		fraction	
0.01410 ±	0.00007	6.78771 ±	0.00393	4.38740 ±	0.02184	1.00462 ±	0.00235
0.02830 ±	0.00014	6.83317 ±	0.00545	2.18595 ±	0.01090	1.01135 ±	0.00269
0.04950 ±	0.00025	7.01739 ±	0.00847	1.24969 ±	0.00643	1.03872 ±	0.00343
0.07780 ±	0.00039	7.19532 ±	0.00618	0.79522 ±	0.00402	1.06471 ±	0.00291
0.11310 ±	0.00057	7.31566 ±	0.00526	0.54712 ±	0.00279	1.08205 ±	0.00287
0.16970 ±	0.00085	7.45195 ±	0.00891	0.36465 ±	0.00184	1.10210 ±	0.00333
0.22630 ±	0.00113	7.49857 ±	0.00827	0.27347 ±	0.00140	1.10874 ±	0.00374
0.31110 ±	0.00156	7.56524 ±	0.00869	0.19892 ±	0.00101	1.11865 ±	0.00348
0.43840 ±	0.00219	7.58119 ±	0.00973	0.14117 ±	0.00071	1.12092 ±	0.00346
0.43850 ±	0.00219	7.57831 ±	0.01876	0.14111 ±	0.00072	1.12093 ±	0.00533
0.60810 ±	0.00304	7.41282 ±	0.01722	0.10175 ±	0.00052	1.09654 ±	0.00471
0.84850 ±	0.00424	6.91732 ±	0.01380	0.07292 ±	0.00037	1.02322 ±	0.00420
1.13140 ±	0.00566	5.99114 ±	0.01045	0.05471 ±	0.00028	0.88519 ±	0.00319

AR 1.00 rotating – DT = 1.99 K – Ra = $1.16 \cdot 10^9$

Rotation rate		Power		Rossby		fraction	
0.02000 ±	0.00010	16.46443 ±	0.00651	4.35182 ±	0.02195	1.00358 ±	0.00123
0.04000 ±	0.00020	16.57937 ±	0.01642	2.17513 ±	0.01102	1.01156 ±	0.00194
0.07000 ±	0.00035	17.00908 ±	0.02494	1.24313 ±	0.00623	1.03735 ±	0.00226
0.11000 ±	0.00055	17.40068 ±	0.00721	0.79115 ±	0.00398	1.06096 ±	0.00125
0.16000 ±	0.00080	17.67213 ±	0.00964	0.54399 ±	0.00274	1.07712 ±	0.00144
0.24000 ±	0.00120	17.89437 ±	0.01719	0.36268 ±	0.00182	1.09052 ±	0.00184
0.32000 ±	0.00160	17.99309 ±	0.00683	0.27200 ±	0.00136	1.09659 ±	0.00116
0.44000 ±	0.00220	17.85807 ±	0.01268	0.19784 ±	0.00100	1.08808 ±	0.00163
0.62000 ±	0.00310	17.64883 ±	0.00634	0.14036 ±	0.00071	1.07615 ±	0.00126
0.86000 ±	0.00430	17.28789 ±	0.01837	0.10119 ±	0.00051	1.05409 ±	0.00204
1.20000 ±	0.00600	16.38436 ±	0.01175	0.07253 ±	0.00037	0.99868 ±	0.00166
1.60000 ±	0.00800	14.75303 ±	0.04460	0.05442 ±	0.00028	0.89846 ±	0.00377

AR 2.00 rotating - DT = 3.99 K - Ra = $2.91 \cdot 10^8$

Rotation rate		Power		Rossby		fraction	
0.00800 ±	0.00010	41.37952 ±	0.03304	21.75392 ±	0.27363	1.00159 ±	0.00130
0.01500 ±	0.00010	41.42181 ±	0.03246	11.60310 ±	0.07925	1.00238 ±	0.00163
0.02400 ±	0.00010	41.52040 ±	0.05198	7.25425 ±	0.03086	1.00388 ±	0.00180
0.03000 ±	0.00020	41.81793 ±	0.00554	5.80539 ±	0.03911	1.01012 ±	0.00061
0.04000 ±	0.00020	42.34256 ±	0.01879	4.35549 ±	0.02188	1.02185 ±	0.00074
0.08000 ±	0.00040	43.82638 ±	0.03096	2.17891 ±	0.01111	1.05610 ±	0.00136
0.14000 ±	0.00070	44.97636 ±	0.05260	1.24584 ±	0.00675	1.08203 ±	0.00326
0.22000 ±	0.00110	45.96892 ±	0.09848	0.79307 ±	0.00457	1.10488 ±	0.00594
0.32000 ±	0.00160	46.77476 ±	0.01213	0.54462 ±	0.00273	1.12776 ±	0.00058
0.48000 ±	0.00240	47.87583 ±	0.02229	0.36311 ±	0.00182	1.15408 ±	0.00084
0.64000 ±	0.00320	48.58329 ±	0.01440	0.27227 ±	0.00138	1.17187 ±	0.00088
0.88000 ±	0.00440	49.26113 ±	0.03218	0.19799 ±	0.00099	1.18857 ±	0.00104
1.24000 ±	0.00620	49.41447 ±	0.01758	0.14051 ±	0.00071	1.19219 ±	0.00080
1.72000 ±	0.00860	47.83159 ±	0.02942	0.10134 ±	0.00051	1.15271 ±	0.00126
2.40000 ±	0.01200	42.92067 ±	0.02674	0.07271 ±	0.00037	1.03097 ±	0.00128
3.20000 ±	0.01600	33.25368 ±	0.02335	0.05461 ±	0.00028	0.79581 ±	0.00092

AR 2.00 rotating - DT = 7.94 K - Ra = $5.80 \cdot 10^8$

Rotation rate		Power		Rossby		fraction	
0.01100 ±	0.00010	100.77677 ±	0.07705	22.32819 ±	0.20409	1.00218 ±	0.00121
0.02100 ±	0.00010	100.72523 ±	0.09795	11.69363 ±	0.05603	1.00216 ±	0.00134
0.03300 ±	0.00020	100.85262 ±	0.05600	7.44334 ±	0.04568	1.00270 ±	0.00111
0.04200 ±	0.00020	101.49866 ±	0.05005	5.85099 ±	0.02818	1.00787 ±	0.00096
0.05660 ±	0.00030	102.76600 ±	0.02492	4.34441 ±	0.02316	1.01872 ±	0.00061
0.11310 ±	0.00060	106.07273 ±	0.01640	2.17536 ±	0.01157	1.04986 ±	0.00046
0.19800 ±	0.00100	108.34789 ±	0.03538	1.24251 ±	0.00629	1.07259 ±	0.00066
0.31110 ±	0.00160	110.18735 ±	0.01432	0.79056 ±	0.00409	1.09169 ±	0.00054
0.45250 ±	0.00230	111.75195 ±	0.01994	0.54340 ±	0.00277	1.10787 ±	0.00051
0.67880 ±	0.00340	113.52353 ±	0.01666	0.36214 ±	0.00182	1.12628 ±	0.00045
0.90510 ±	0.00450	114.67356 ±	0.01846	0.27165 ±	0.00135	1.13710 ±	0.00049
1.24450 ±	0.00620	114.95585 ±	0.02655	0.19753 ±	0.00099	1.14049 ±	0.00065
1.24450 ±	0.00620	115.21135 ±	0.03518	0.19755 ±	0.00100	1.14262 ±	0.00106
1.75360 ±	0.00880	115.28948 ±	0.01573	0.14025 ±	0.00071	1.14235 ±	0.00060
2.43240 ±	0.01220	113.05606 ±	0.06323	0.10112 ±	0.00052	1.11985 ±	0.00127

AR 2.00 rotating - DT = 15.81 K - Ra = $1.16 \cdot 10^9$

Rotation rate		Power		Rossby		fraction	
0.01500 ±	0.00010	245.77982 ±	0.18778	23.10724 ±	0.15513	1.00310 ±	0.00118
0.03000 ±	0.00020	245.34124 ±	0.12866	11.55157 ±	0.07761	1.00178 ±	0.00096
0.04700 ±	0.00020	245.56901 ±	0.07253	7.37462 ±	0.03177	1.00225 ±	0.00073
0.06000 ±	0.00030	247.46642 ±	0.29758	5.78055 ±	0.03017	1.00825 ±	0.00232
0.08000 ±	0.00040	249.91901 ±	0.11059	4.33872 ±	0.02180	1.01617 ±	0.00078
0.16000 ±	0.00080	257.85551 ±	0.01752	2.17088 ±	0.01088	1.04649 ±	0.00035
0.28000 ±	0.00140	263.14145 ±	0.03101	1.24044 ±	0.00621	1.06808 ±	0.00041
0.44000 ±	0.00220	265.98509 ±	0.01396	0.78901 ±	0.00395	1.08095 ±	0.00033
0.64000 ±	0.00320	268.89884 ±	0.04308	0.54230 ±	0.00272	1.09355 ±	0.00047
0.96000 ±	0.00480	272.41919 ±	0.03592	0.36139 ±	0.00181	1.10906 ±	0.00047
0.96000 ±	0.00480	272.22867 ±	0.05193	0.36139 ±	0.00182	1.10827 ±	0.00061
1.28000 ±	0.00640	272.60068 ±	0.05764	0.27101 ±	0.00136	1.11010 ±	0.00056
1.76000 ±	0.00880	270.86317 ±	0.04067	0.19720 ±	0.00099	1.10158 ±	0.00054
2.48000 ±	0.01240	268.26684 ±	0.03459	0.13993 ±	0.00071	1.09143 ±	0.00077
3.44000 ±	0.01720	264.51389 ±	0.07402	0.10090 ±	0.00051	1.07565 ±	0.00076

Appendix B: Photos

B.1 Construction

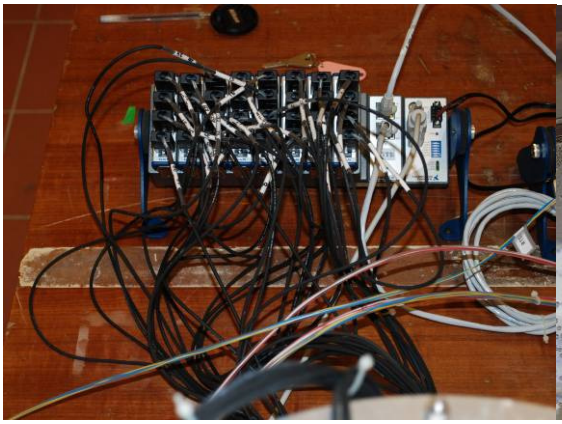
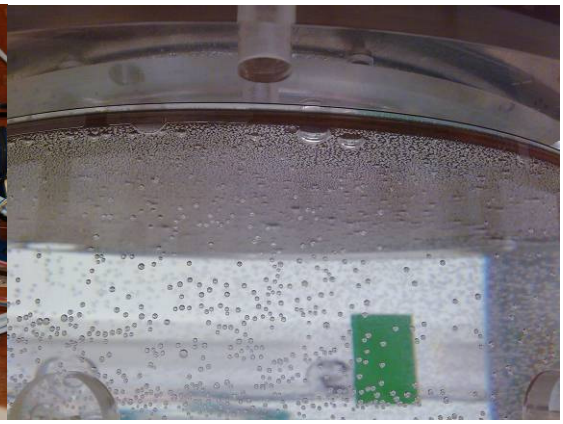

The sensor wiring towards the NI-cRIO for the Γ=1 setup (left).
A thin layer of air bubbles formed on the top plate when degassing the water before starting the experiments (right).


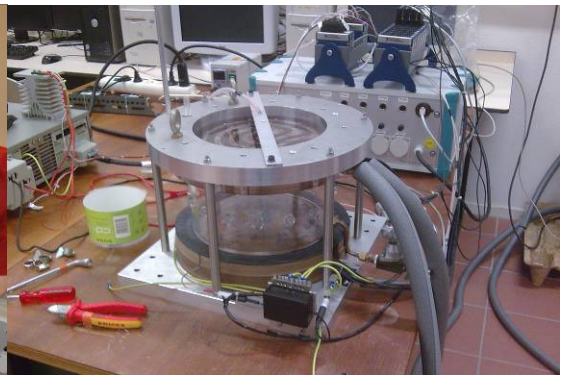

From left to right: Gerald, Eric, Freek, Ad and Richard working on the assembly of the Γ=1 setup (left).
The Γ=2 setup without sidewall sensors, isolation or water (right).

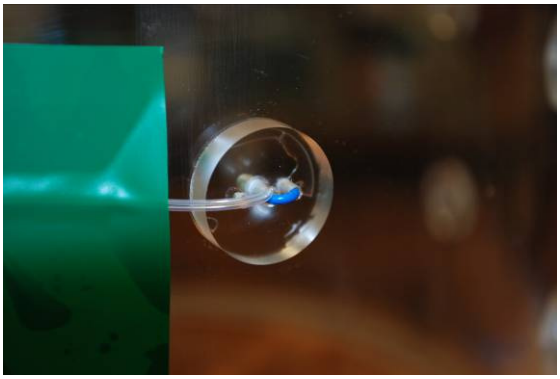
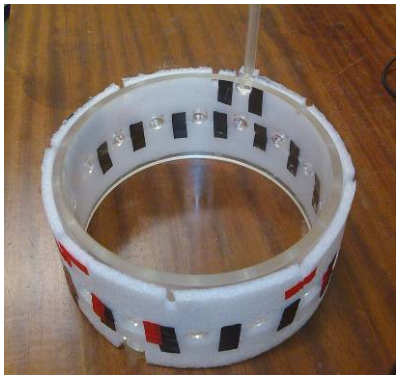

The sidewall sensors are fixated in their holes with wire-isolation, while their measurement wires are guided with adhesive tape (left).
The Γ=2 sidewall with its first layer of isolation (right).

B.2 Measurements on the Rotating Table Facility

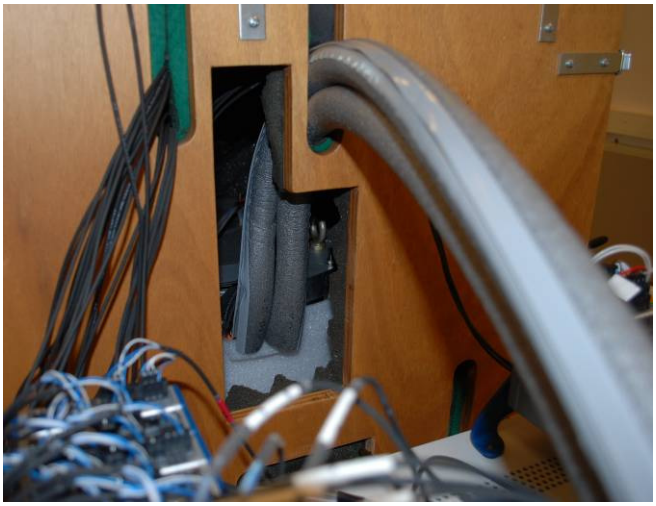
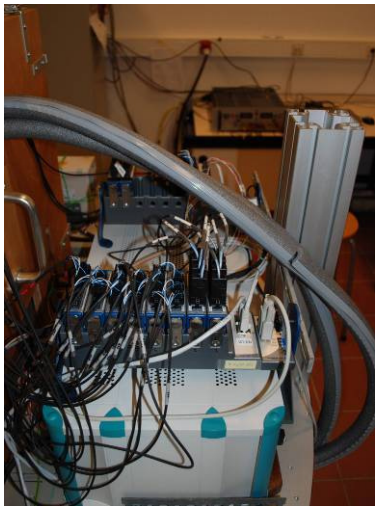

The Γ=2 setup is visible inside its insulating box after removing the handle (left).
Each sensor has a separate, 3-wire cable and connector on the NI-cRIO system (right).

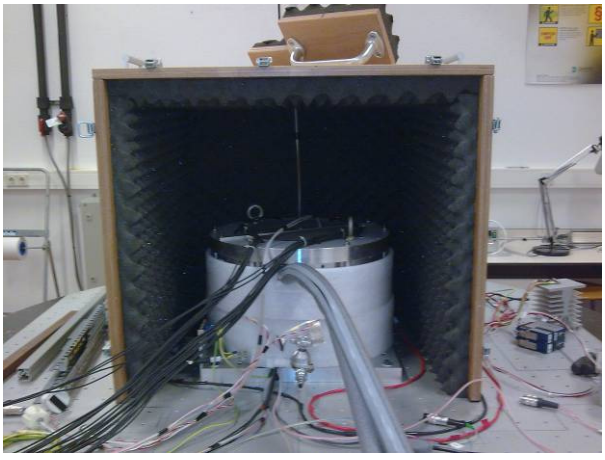
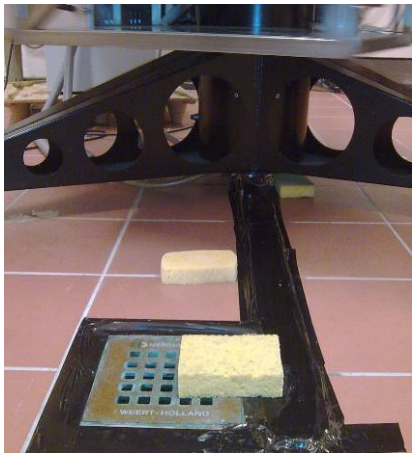

The Γ=2 setup inside the insulating box at the end of the experiments (left).
A water guide was made out of tape and isolation fabric on the floor below the RTF to guide at least some of the lost coolant water to a higher point in the lab (right).